Results in Engineering 27 (2025) 106728

Contents lists available at ScienceDirect

Results in Engineering

journal homepage: www.sciencedirect.com/journal/results-in-engineering

Research paper

Analysis of piezoelectric harvester with multi-array configuration for ultra-low power sensor nodes

Lydia Schott [a,*], Ghada Bouattour [c], Robert Fromm [a], Florian Strakosch [a], Olfa Kanoun [b], Faouzi Derbel [a]

[a] Smart Diagnostic and Online Monitoring, Leipzig University of Applied Sciences, Wächterstraße 13, Leipzig, 04107, Saxony, Germany
[b] Measurement and Sensor Technology, Chemnitz University of Technology, Reichenhainer Straße 70, Chemnitz, 09126, Saxony, Germany
[c] Institute for Production Technology and Systems, Leuphana University Lüneburg, Universitätsallee 1, Lüneburg, 21335, Lower Saxony, Germany

ARTICLE INFO

Keywords:
Piezo harvester
Multi-array piezo
Wake-up receiver sensor node
Wireless sensor network

ABSTRACT

Autonomous wireless sensor networks (WSNs) have been identified as playing a crucial role in monitoring applications in hard-to-access and industrial environments. This study presents a comprehensive investigation of multi-piezoelectric configurations, including series, parallel, and hybrid configurations, for vibration-based energy harvesting in wake-up receiver (WuRx) nodes, with a particular focus on the gearbox of bucket wheel excavators. A novel analytical model has been developed to predict the electrical behaviour and power output of identical piezoelectric elements under various connection schemes and operating conditions. The experimental validation of the model yielded maximum deviations of 14 % in the load power and 9 % in the impedance estimates, thereby underscoring the model's reliability. A total of ten distinct configurations were evaluated, each comprising four piezoelectric elements. The four-in-parallel (0S4P) arrangement was found to demonstrate superior performance by enabling supercapacitor power peaks of 75 mW, representing the peak instantaneous power stored in the capacitor and sustained over 240 ms. These outcomes emphasise the potency of optimised piezoelectric configurations in facilitating autonomous, self-sufficient WuRx-enabled sensor nodes. The findings offer critical insights for designing resilient, energy-autonomous WSNs tailored for predictive maintenance and monitoring in high-vibration industrial environments.

1. Introduction

In recent times, there has been a notable increase in the deployment of sustainable wireless sensor networks (WSNs) within a variety of monitoring applications. This is largely attributable to their capacity to gather data from remote or inaccessible regions without the requirement for wired connections. In the domain of environmental monitoring, these devices play a pivotal role. They are utilised to monitor parameters such as temperature, humidity, air and water quality, and pollution levels in various ecosystems, including forests, oceans, and urban environments [1]. In the domain of smart agriculture, WSNs facilitate precision farming through the monitoring of soil moisture, temperature, and plant health. This assists in optimising irrigation, controlling pests, and enhancing yields while conserving resources [2].

In smart cities, WSNs facilitate real-time data collection and communication across urban systems, enhancing efficiency, sustainability, and resource management to meet long-term social, economic, and environmental objectives [3]. In the field of healthcare, wireless sensors have been utilised for the purpose of monitoring vital signs, patient mobility, and environmental conditions. This is facilitated through the utilisation of wearable devices that are equipped with the capability to transmit the gathered data to designated user applications. This approach enables remote monitoring, which is a significant advancement in healthcare monitoring and management.

WSNs have also been employed for indoor localisation, with the purpose of tracking objects or people within buildings. This has been demonstrated to facilitate warehouse logistics and indoor navigation [4]. In industrial contexts, these sensors facilitate predictive maintenance by monitoring parameters such as temperature, pressure, and vibration, thereby reducing downtime and enhancing safety [5].

---

* Corresponding author.
E-mail addresses: lydia.schott@htwk-leipzig.de (L. Schott), ghada.bouattour@leuphana.de (G. Bouattour), robert.fromm@htwk-leipzig.de (R. Fromm), florian.strakosch@htwk-leipzig.de (F. Strakosch), olfa.kanoun@etit.tu-chemnitz.de (O. Kanoun), faouzi.derbel@htwk-leipzig.de (F. Derbel).

https://doi.org/10.1016/j.rineng.2025.106728
Received 18 April 2025; Received in revised form 11 August 2025; Accepted 12 August 2025

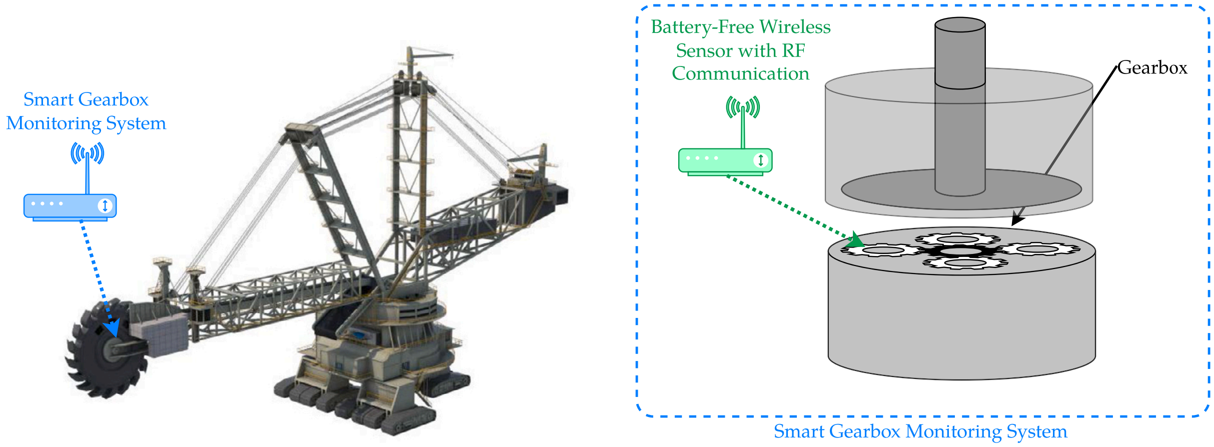

(a) Application of wireless sensor in an excavator.

(b) Position of wireless sensor inside excavator gearbox.

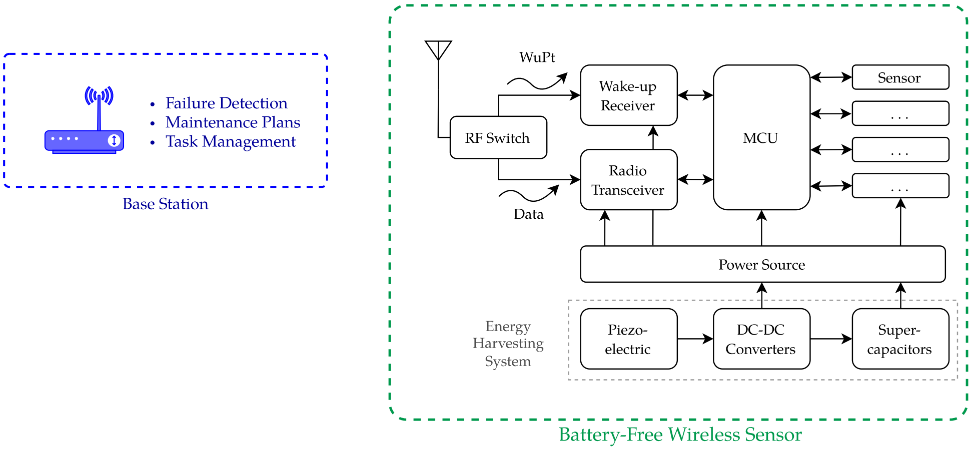

(c) Base station needed as edge connection for wireless sensor.

(d) Wireless sensor building blocks.

Fig. 1. Illustration of wireless sensors and vibration-based energy harvester in an excavator gearbox.

However, despite these advantages, WSN devices are confronted with significant challenges, including high energy consumption, particularly due to the continuous active listening feature, which results in a reduction in battery life [6]. Duty-cycling schemes have been demonstrated to reduce power consumption; however, they frequently result in increased latency and compromised data timeliness.

In order to address issues of energy constraints, sustainable WSNs have been developed to leverage battery-free designs that are powered by energy harvesting [7] or wireless charging [8], with energy stored in supercapacitors. As demonstrated in Fig. 1a, the utilisation of sustainable nodes has been shown to be advantageous for applications such as gearbox fault detection. This assertion is supported by the works of [9] and [10].

The selection of an appropriate energy supply for wireless sensor node (WS) is contingent upon application-specific requirements, energy demands, and the availability of suitable energy sources [11,12]. The harvesting of ambient energy has been identified as a strategy that is both environmentally friendly and conducive to the extension of the lifespan of devices. In addition, this approach has been shown to engender a reduction in recycling costs when compared with conventional batteries. A wide variety of energy sources and transducers are employed, including solar cells [13], thermoelectric generators [14], and vibration harvesters. In industrial environments, mechanical energy is particularly abundant and can be converted using electrostatic [15], electromagnetic [16], or piezoelectric [17] methods.

Among these options, piezoelectric energy harvesters (PEHs) are particularly promising owing to their widespread availability, mechanical durability, rapid response, and high power density [18–20]. The function of the PEHs is to convert ambient vibrations into electrical energy. This process serves to prolong the operational lifetime of sensor nodes and support long-term monitoring without the need for frequent manual maintenance. In order to enhance the harvested energy output and system reliability, piezoelectric elements (PZs) can be arranged in series, parallel, or hybrid configurations. The selection of an optimal multi-array piezoelectric energy harvester (MPEH) configuration necessitates a balanced consideration of the voltage, current, and total power in order to meet the specific requirements of the given application.

However, relying on a single PEH may not ensure a stable and sufficient energy supply. Recent research has explored the potential of advanced PZ designs and hybrid harvesters that combine piezoelectric and electromagnetic converters with a view to enhancing output [21–27]. Furthermore, active rectifier circuits, including the synchronized switch harvesting on inductor (SSHI) and synchronous electric charge extraction (SECE), have the capacity to enhance power extraction efficiency. However, they also introduce complexity and frequently result in the necessity for additional power supplies [28,29].

The integration of a secondary radio interface, designated as a wake-up receiver (WuRx), has been identified as a pivotal strategy to effectively minimise the overall power consumption in wireless sensor networks. The WuRx device is capable of detecting a specific wake-up signal, thereby ensuring that the main transceiver is activated solely when required. This function significantly reduces losses due to idle listening [30,31]. This architecture facilitates the implementation of energy harvesting as a viable supply method, even for low-power nodes [32].

For instance, nodes equipped with the WuRx system can be mounted on industrial machinery to continuously monitor vibrations and other parameters with minimal maintenance requirements.

Recent advances in ultra-low-power wireless sensor networks have highlighted the complementary but distinct roles of RF energy harvesting (RF-EH) and WuRx architectures. It is evident that RF-EH systems generally necessitate incident RF power levels of approximately −30 dBm or higher to operate within the rectifier's linear region, where RF-to-DC conversion efficiency becomes feasible. For instance, practical rectennas achieve an efficiency of over 40 % at −10 dBm and maintain functionality down to approximately −20 dBm. However, they encounter difficulties below −30 dBm [33]. In contrast, WuRx circuits are engineered to detect extremely weak RF signals, often below −60 dBm, by leveraging the square-law region of the rectifier characteristic to maximise sensitivity. Some implementations have been reported to achieve detection thresholds as low as −61.6 dBm at microwatt-level power consumption [34]. This operational contrast highlights the inherent trade-off between maximising the harvested power and achieving a high sensitivity for reliable wake-up signal detection in ambient RF environments.

The selection of the optimal configuration for a MPEH system necessitates a comprehensive evaluation of the merits and demerits of three distinct configurations: series, parallel, and hybrid. Each of these configurations influences the power, voltage, and current output of the system. The present study focuses on the design and testing of an MPEH system that has the capacity to reliably power a sensor node with a WuRx, which is utilised for the purpose of monitoring the condition of a coal excavator gearbox. The objective is to establish an efficient configuration and to validate its performance through experimental analysis. The remainder of this paper is structured as follows: Section 2 provides a review of the existing literature concerning MPEH systems and their application with sensor nodes. Section 3 elaborates on the proposed methodology, including the design of the WuRx and the gearbox's operational range. Section 4 offers a comprehensive presentation of the MPEH model. Section 5 details the practical implementation and testing of the system within the context of gearbox monitoring. Section 6 discusses the experimental findings and possible enhancements, while Section 7 offers a conclusion to the paper and outlines prospective future research directions.

2. Related works

It is evident that PEH has attracted considerable attention as a means to facilitate self-powered WSNs, particularly within industrial contexts where uninterrupted monitoring is crucial but battery maintenance is impractical. A substantial body of research has evidenced the feasibility of utilising mechanical vibrations as a means of generating power for sensor nodes by employing piezoelectric transducers [35–41]. The reported power outputs exhibit a substantial range, spanning from approximately 1.3 mW to over 20 W. This observation underscores the potential of PEH to sustain low-power devices under variable conditions.

As demonstrated by other researchers, there is a clear shift towards high-fidelity modelling and advanced material integration, which are used to address the limitations of classical methods. [42] employed a nonlocal coupled stress meshless model to assess microscale effects in nanocomposite beams, while [43] used a strain gradient Kriging method to analyse the thermo-electro-mechanical stability in graded microshells. As demonstrated by [44], there has been an advancement in the field of shell modelling through the utilisation of isogeometric Reissner-Mindlin formulations. In the present study, recent progress in geometric design and multi-physics optimisation is synthesised by [45].

A crucial strategy for enhancing the efficiency and flexibility of PEH is the implementation of multi-array configurations. The arrangement of PZ in a series configuration has been demonstrated to result in an enhancement of voltage output, while the parallel configuration has been shown to yield an increase in current output [46–50]. Consequently, the configuration of combined series-parallel topologies can be adapted to satisfy particular load requirements through the optimisation of voltage, current, and impedance characteristics. However, extant models are principally concerned with theoretical and experimental analyses, rather than providing a unified framework for selecting the optimal number of elements and their interconnections under diverse operating conditions [51–54].

In order to facilitate effective power transfer from the harvester to the load, it is essential to ensure that impedance matching is carried out with the appropriate degree of care. The ideal load would counterbalance the capacitive nature of piezoelectric devices through complex conjugate impedance. However, this is impractical due to the need for excessively large inductances [55]. Consequently, resistive loads are typically employed, with the maximum power transfer being achieved by matching the resistance to the Thevenin equivalent impedance [56]. However, the presence of dynamic variations in load conditions poses additional challenges for the practical design of circuits [57].

A number of studies have been conducted on multi-array piezoelectric structures with a view to enhancing energy harvesting efficiency. For instance, [58] conducted simulations to demonstrate the performance benefits of different array configurations, although experimental validation was lacking. Li et al. [52] investigated adaptive beamforming with multi-array piezo-ceramic structures, by employing a P-SSHI rectifier to improve efficiency. However, practical limitations such as parasitic losses and circuit complexity were not fully addressed. In a similar context, research by [59] and [60,61] analysed hybrid configurations and footstep-based harvesting. However, these studies focused on predefined setups and did not offer a systematic method for determining optimal combinations. A comprehensive comparison of the reviewed multi-array piezoelectric energy harvesting configurations is provided in Table 1.

Despite the valuable contribution of [62] in developing equivalent circuit models for series, parallel, and series-parallel PEH configurations, their experimental validation is limited to series and parallel cases tested separately. The absence of direct testing on actual serial-parallel arrays leaves the potential effects and impedance interactions unverified. While [63] provide a comprehensive analysis of the aerodynamic and mechanical interactions in MPEH arrays, their experimental validation of electrical configurations is limited to purely series or parallel connections within sub-arrays. However, the investigation did not extend to fully integrated series-parallel electrical interconnections.

It is evident that, despite these advances, the majority of investigations remain confined to the harvester structures. However, there was no extension to integrated end-to-end systems combining multi-array harvesters with fully functional sensor nodes and advanced energy management strategies. It is noteworthy that the incorporation of WuRx has been identified as a potentially effective approach for significantly reducing standby energy consumption in WSNs. The primary function of WuRx architectures is to activate sensor nodes only when necessary, thereby mitigating idle power drain. This is a critical concern for low-duty-cycle applications, such as gearbox condition monitoring.

A body of research that has been conducted in parallel has demonstrated the feasibility of piezoelectric-powered sensor nodes under real-world conditions. For instance, the works of [64] and [65] illustrate how single or multiple cantilever configurations can sustain sensor nodes through optimized power management. In addition, studies such as [66,67] explored buffering and scheduling techniques, while [68–70] highlighted the benefits of ultra-low-power modes and simple wake-up strategies. However, these implementations primarily rely on single-element or basic stacked configurations, which limits their adaptability to complex vibration sources and variable mechanical inputs. As outlined Table 2 outlines key studies on PEH supplying WSs are summarised.

In summary, significant progress has been made in both MPEH and energy-autonomous WSs. However, to the best of the author's knowledge, no existing study has demonstrated a combined system that in-

Table 1

Characteristics of MPEH Approaches: Array Configurations, Operating Vibration Frequencies, Output Performance, and Load Resistance Parameters.

Ref.	array variations	vibration frequency (Hz)	energy output (mW)	rectifier	resonant circuit	load resistance (kΩ)
[51]	2S1P, 1S2P, 1P, 2P, 3P, 1S, 2S	3	0.597	FBR	P-SSHI	10 - 1000
[60]	8P, 8S, 6S2P, 2S6P	0.5	12.3	n. A.	n. A.	0.001 - 0.680
[61]	10 not specified	n. A.	0.242	n. A.	n. A.	0.140 - 0.280
[52]	8S1P, 4S2P, 2S4P, 1S8P	200	0.017 - 0.100	FBR	P-SSHI	1000
[59]	1P, 2S1P, 3S1P 2P1S, 3P1S	68	5.05	AC	AC	4.5
[58]	1S2P	1	0.0035	AC	AC	1000
This work	1P, 2P, 3P, 4P, 1S1P, 2S1P, 3S1P, 1S2P, 2S1P, 1S3P	63 Hz	2.85	FBR	-	1 - 1000

Table 2

Components of a Sensor Node with PEH: Vibration Frequency Range, Rectifier Type, and Energy Storage Elements.

Ref.	Carrier Frequency (MHz)	Trans-ceiver	Micro-controller	Vibration Frequency (Hz)	Number of PZ	Rectifier Converter	Energy Storage (mF)
[64]	2450	CC2650	CC2650	64 - 78	3	LTC333	470
[65]	2450	CC2530	STM32	100	3	3x LTC 3588	16
[66]	868	LoRaWAN	RFM95	100–250	5	LTC3588	4.7
[71]	2450	n.A.	MBS-6003z	60-150	1	LTC3331	10
[70]	868	CC1100	Atmega32L	20	1	n.A.	150
[69]	2450	CC2530	CC2530	100	1	LTC3106	0.680
[68]	2450	CC2530	CC2530	25	1	LTC3588-1 & LTC3505	15
[67]	2450	NRF51822	MSP430	22.3	1	LTC3588-1	4.66
This work	868	SPIRIT1	MSP430	63	4	LTC3588	3

tegrates a MPEH with a dedicated WuRx-enabled sensor node. Such integration is especially critical for applications such as gearbox condition monitoring, where variable mechanical input, selective sensing, and ultra-low-power standby operation are required simultaneously.

In order to address this gap, the present study proposes a novel integrated solution that combines a robust MPEH architecture with a sensor node that is equipped with a WuRx. The novel approach is evaluated through the development of a prototype in a laboratory setting. The objective is to ensure stable, maintenance-free, and battery-less operation in realistic industrial conditions by maximising the harvested energy and minimising the wasted standby power. The system under discussion represents a significant advance in the field of industrial gearbox monitoring, due to its capacity for practical, long-term, self-sustained monitoring.

3. Proposed approach and methodology

The present study investigates the utilisation of the WSNs equipped with WuRxs for the purpose of monitoring the condition and predicting the maintenance requirements of a bucket wheel excavator gearbox. The vibrations generated by the machine are harnessed by PEHs to power these components. The combination of series and parallel circuits has been demonstrated to enhance the sustainability of wireless sensor systems. In selecting the number of PZs, a number of challenges must be given full consideration. Chief among these is the stability of the system in the face of element failure, as well as the requisite energy and power. Consequently, particular aspects and selection strategies should be given due consideration. The implementation of this process necessitates the utilisation of a bespoke design model, which facilitates the selection of the parameters of series or parallel PZ. In addition, a variety of series and parallel AC/DC combinations are feasible, ensuring the requisite power level is attained. In order to reduce the losses of the combined connection, identical PZs are excited with the same frequency and acceleration, where no current of one PZ is supplied to the others.

Initially, the vibration frequency, acceleration, size and energy consumption profile of the WSN must be defined. Subsequently, the appropriate selection of PZ is made, alongside their specific characterisation with regard to the application vibration profile. In view of the preceding data, it is necessary to execute estimations of possible PZ numbers and combinations by means of the proposed model. The proposed analytical model illustrates the output power and voltage, taking into account the equivalent load impedance, which is defined as the average energy consumption. The developed analytical model was then subjected to experimental verification. This was achieved by carrying out all possible combinations of a case of four PZs.

The utilisation of vibrations in industrial machinery necessitates the employment of piezoelectric bending beams, which are the optimal solution for this purpose. The bending beam can be adapted for specific applications, rendering it an exceptionally versatile actuator. The compact design of the piezoelectric bending beam enhances its appeal for technical applications. Moreover, the elevated reliability of the device under discussion has been shown to engender a marked reduction in

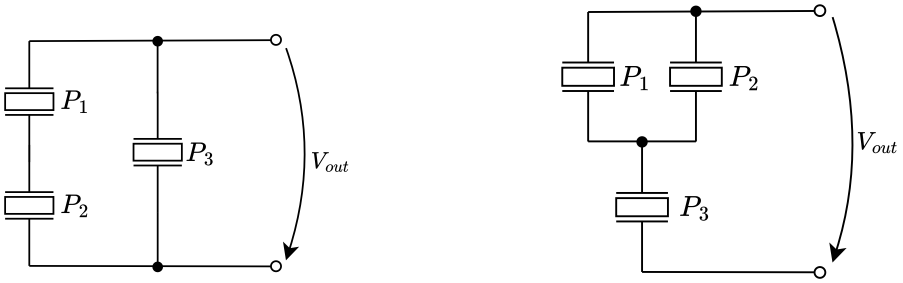

(a) Serial configuration approach of MPEH.

(b) Parallel configuration approach of MPEH.

Fig. 2. MPEH configuration approach in two variants.

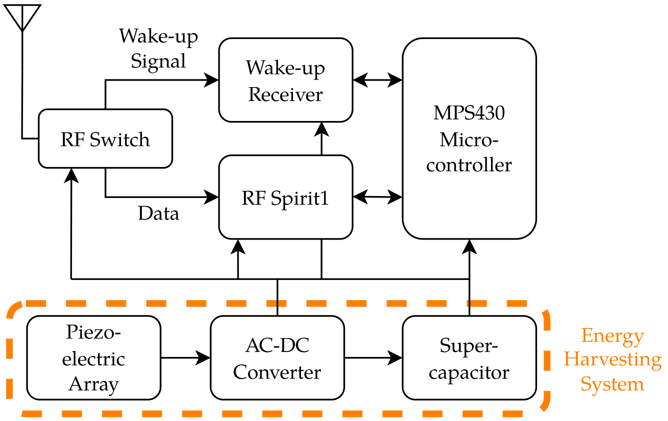

Fig. 3. Proposed sensor node with piezo electric power supply.

downtime, with disruptions becoming a rare occurrence [72]. As illustrated in Fig. 2a, two PZs are linked in series, with one additional PZ connected in parallel. This configuration is regarded as robust due to the fact that the failure of a single PZ does not result in the failure of the entire generator.

However, it should be noted that the configuration of the array, as illustrated in Fig. 2a, is not without its limitations. Specifically, the voltage is constrained by a single PZ in parallel, thereby impeding any potential enhancement in performance that might be achieved through the connection of multiple PZs. Conversely, the configuration of figure Fig. 2b, exhibits two PZs arranged in parallel and a single PZ arranged in series. Despite its reduced robustness, a failure in the series-connected PZ results in a complete cessation of power generation and the absorption of all power by the weaker PZ. However, it offers the advantage of unrestricted voltage. Therefore, the utilisation of multiple piezos in this configuration has been demonstrated to enhance power output, as evidenced by the works of [58] and [63].

3.1. *Wake-up receiver system design*

It has been demonstrated that WuRx has gained recognition as an effective mechanism for supporting asynchronous communication within WSN. The technology, known as WuRx, when implemented in wireless sensor nodes, offers several advantages, primarily concerning energy efficiency, reduced delays, improved reliability, and enhanced scalability within the WSN. Firstly, WuRx technology conserves energy by enabling sensor nodes to spend the majority of their time in a low-power sleep state. This results in a significant reduction in energy consumption when compared with traditional methods. This contributes to the prolongation of the operational longevity of battery-powered sensor nodes, thereby rendering them suitable for long-term deployment in remote areas [73]. Secondly, the WuRx technology has been demonstrated to reduce delays by enabling sensor nodes to rapidly initiate activity in response to specific signals or events, thereby ensuring the timely transmission of data. This is of particular importance for applications that necessitate real-time monitoring and control.

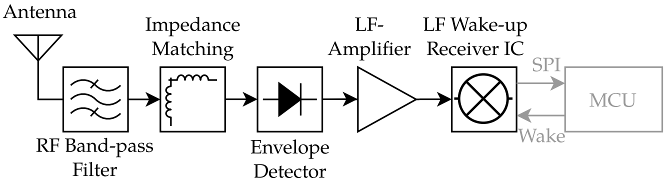

Fig. 4. Block diagram of the WuRx architecture.

Furthermore, the WuRx technology enhances network reliability by reducing the probability of missed or delayed transmissions. It has been demonstrated that nodes are capable of promptly activating upon reception of the signal wake-up packet (WuPt), thereby mitigating the risk of interruptions in data transmission, even in challenging environments [74]. Furthermore, the technology in question supports network scalability, allowing the deployment of large-scale wireless sensor networks with numerous nodes across wide areas. As demonstrated in [75], a reduction in energy consumption has been shown to facilitate denser node deployments and broader network coverage without compromising performance.

It is imperative that event-driven communication is employed in order to ensure the timely identification of any malfunctions in the gearbox system of a coal excavator. The excavator exhibits a range of operational states, including idling, light, and heavy loads. These states are identified by the data collection unit located on the exterior of the gearbox, owing to its connection to the excavator's control system. The measurement phases for the sensors were initiated by triggering events. It has been determined that the power consumption of standard RF transceivers exceeds 10 mW, thus rendering idle listening for sensors a non-viable option. In order to address this issue, the use of an ultra-low power WuRx is employed, which exhibits negligible power consumption below 20 µW, thereby facilitating event-driven communication.

The WuRx model adheres to the architectural framework delineated in [76]. As illustrated in Fig. 3, the proposed architecture is depicted as a block diagram. The device under consideration contains the SPIRIT1 as the primary radio for communication and data transmission, and a 16-bit MSP430G2553 as the primary microcontroller. The energy generated by the PEH is then utilised to supply the WuRx via a storage capacitor.

The fundamental components of this framework are illustrated in Fig. 4. The architecture is characterised by a passive front end, which is employed to convert the RF signal into the LF. In order to circumvent the potential for interference from extraneous systems, the implementation of an RF band-pass filter is incorporated into the WuRx input. It has been demonstrated that the sensitivity of the entire design is increased by amplifying the LF signal with a corresponding amplifier built out of bipolar junction transistors (BJTs).

The AS3933 LF wake-up receiver IC is responsible for the detection of the WuPt. The system is capable of detecting packets within the 18.7 kHz

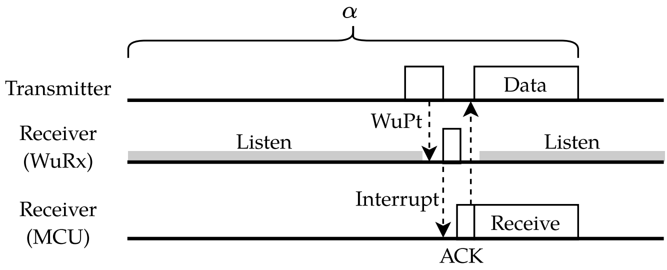

Fig. 5. Signal timings of wake-up interval.

range and performing an address match, as outlined in the study by [34]. In the event of a match, an interrupt signal is dispatched to the MCU. Thereafter, the sensor data are transmitted to the central unit via the radio module (SPIRIT). The active period is restricted to a few milliseconds for data exchanges. It is evident that the MCU and SPIRIT subsequently enter a state of sleep mode. The operating principle of the WuRx over a wake-up interval alpha is illustrated in Fig. 5. In order to ensure the efficacy of these operational behaviours, it is imperative that the minimum requisite input power of the energy-harvesting source exceeds the energy consumption during the listening mode.

3.2. Gearbox working band

The optimal performance of the PEHs is dependent on its resonance frequency range; therefore, the determination of the gearbox's frequency range is essential for the selection of suitable PEHs. In order to achieve this objective, it is necessary to position sensor nodes equipped with acceleration sensors, which have been specifically designed for low-frequency measurements, within the gear wheel. This approach is outlined in the work of [77]. As demonstrated in Fig. 6a and Fig. 6b, the sensor placement within the gearbox is of paramount importance. These sensors are connected to the MSP430 microcontroller, which enables data transmission to a central receiver unit via the SPIRIT1 RF module. Data spanning 36 s, capturing the acceleration under varying load conditions, is recorded for each sensor. The analysis is undertaken using a fast Fourier transformation, which reveals distinct modes of the gearbox [10,78].

The response of an excavator to varying mechanical loads results in distinct vibrational characteristics. When the gearbox is subjected to a high load (refer to Fig. 7a), two prominent frequency bands emerge at 1.91 Hz and 60 Hz, each with a notable amplitude of approximately 0.03 g. In contrast, under low load conditions (refer to Fig. 7b), only the 60 Hz frequency demonstrates a heightened acceleration level of 0.025 g. The PZs has been demonstrated to generate significant energy across a range of standard operating conditions, thereby validating the selection of the 60 Hz frequency as the primary operational frequency for the PEH.

4. Piezoelectric harvester array system

4.1. Basics of piezoelectric within cantilever beam

The piezoelectric effect is the process by which mechanical stress is directly converted into electrical charge. This is due to the asymmetrical crystal lattice of piezoelectric materials [79]. The resulting open-circuit voltage is determined by the coupling between the mechanical loading and electrical polarization.

The associated electrical voltage is defined by the following relationship

$$V_{\mathrm{piezo}} = \frac{d_{\mathrm{ij}} \cdot F}{C} \tag{1}$$

The term was coined by [80]. In this context, the symbol F represents the mechanical force acting, C denotes the electrical material capacitance, and d is the direction-dependent piezoelectric charge constant.

For a cantilever beam operated in the transverse d_{31} mode, the relevant constitutive relationship is expressed as follows [81,82]:

$$\begin{aligned} D_3 &= d_{31} T_1 + \epsilon_{33}^{T} E_3 \\ S_1 &= s_{11}^{E} T_1 + d_{31} E_3 \end{aligned} \tag{2}$$

where T_1 denotes the axial stress induced by bending, D_3 signifies the transverse electric displacement, E_3 represents the electric field across the piezoelectric layer thickness t_p, d_{31} is the transverse piezoelectric coefficient, ϵ_{33}^{T} is the transverse permittivity at constant stress, and s_{11}^{E} is the axial elastic compliance at a constant electric field.

In the context of open-circuit conditions, it can be deduced that the dielectric displacement is rendered null ($D_3 = 0$), thus giving rise to

$$E_3 = -\frac{d_{31}}{\epsilon_{33}^{T}} T_1. \tag{3}$$

The open-circuit voltage across the piezoelectric layer can be expressed as:

$$V_{OC} = E_3 \cdot t_p = -\frac{d_{31} \cdot t_p}{\epsilon_{33}^{T}} T_1. \tag{4}$$

As demonstrated in Fig. 8, for a bending cantilever, the d_{31} mode pertains to the scenario in which the axial stress resulting from bending instigates a transverse electric field, consequently leading to a harvestable voltage [83–85]. This model forms the basis for estimating the piezo-generated voltage in practical vibration energy-harvesting applications.

4.2. Modeling of multi-array piezoelectric energy harvesters system

The development of a piezoelectric energy harvester is represented by its Thevenin equivalent, which is defined as a voltage source in series with a capacitance and a resistive load. In the event of excitation at either the electrical or mechanical port, the two-port piezoelectric system can be reduced to a single-port equivalent consisting of a Thevenin generator and impedance [86].

The open-circuit voltage, denoted by V_{OC}, is a measure of the dynamic response of the cantilever to external excitations, such as applied force and acceleration. The resonant frequency and output voltage are critical parameters for selecting suitable PZs, as stipulated in the datasheets provided by the manufacturers. The simplified equivalent circuit for energy harvesting is presented in Fig. 9, comprising the voltage source V_{OC}, the capacitive impedance Z, and the load resistance R_L.

The capacitance impedance, denoted

$$Z = \frac{1}{j\omega C_0} \tag{5}$$

exhibits a frequency-dependent variation, thereby causing the fraction of the load voltage to also vary.

In order to enhance the harvested power, it is possible to interconnect several PZs in either a series or parallel configuration. As [58] demonstrate, the configuration of multiple PZs can be divided into the following combination possibilities: fully series, fully parallel, and a combined series and parallel architecture. The development of an equivalent circuit for the piezoelectric array architecture is founded upon the fundamental model and the successful simulation. The model is based on a voltage source connected to an equivalent impedance in series, and from Eq. (5)is obtained, as illustrated in Eq. (6). The symbol Z_s is employed to denote the number of PZs that are connected in series.

$$Z_s = \frac{1}{j\omega C} \cdot s \tag{6}$$

with s as the number of PZ connected in series.

(a) Bucket wheel of the excavator for gearbox monitoring.

(b) Detailed view of the excavator gearbox.

Fig. 6. Construction of gearbox and WS for condition monitoring on the bucket wheel excavator.

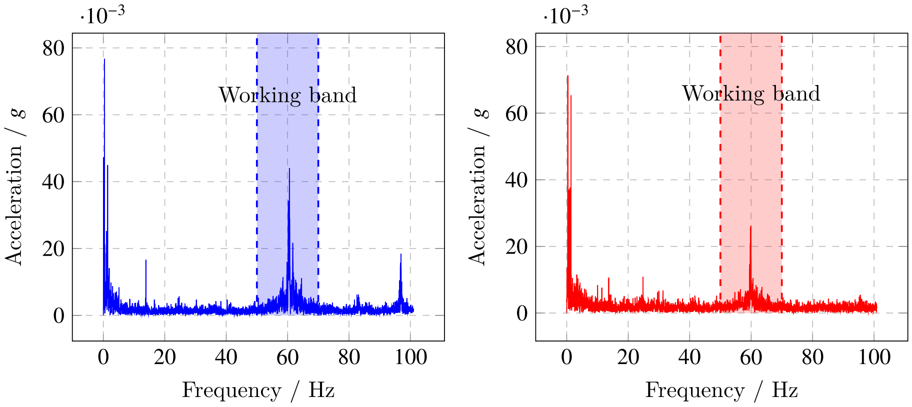

(a) Acceleration for high load.

(b) Acceleration for low load.

Fig. 7. Real measurement of acceleration from excavator gearbox.

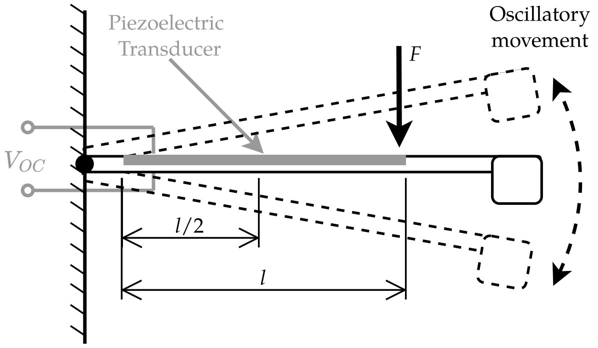

Fig. 8. Schematic of a piezoelectric bimorph cantilever beam with a tip mass for harvesting energy from vibrations.

The model proposed in this study intentionally isolates the electrical dynamics from the mechanical aspects of the PEH system, focusing exclusively on the electrical domain [62]. However, this deliberate decoupling, however, introduces additional layers of uncertainty, which are addressed by incorporating a corrective adjustment parameter, designated here as c.

The voltage with factor V_{OC} is given by the equation

$$V_0 = V_{\mathrm{OC}} \cdot c \tag{7}$$

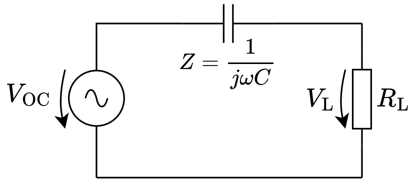

Fig. 9. Equivalent circuit representation of the piezoelectric transducer with a resistive load.

The equivalent voltage V_{s} of the circuit is defined as the voltage sources V_0 which are connected in series.

$$V_{\mathrm{s}} = V_0 \cdot s \tag{8}$$

In the event of the equivalent piezoelectric circuits being connected in parallel, an equivalent impedance of

$$Z_{\mathrm{p}} = \frac{1}{j\omega C} \cdot \frac{1}{p} \tag{9}$$

is observed, with p denoting the number of PZs connected in parallel.

It can be demonstrated that the equivalent voltage

$$V_{\mathrm{p}} = V_0 \tag{10}$$

of the circuit is equal to the voltage source for parallel connected PZ (V_{p}). The term $V_0$is used to denote a single PZ voltage. According to Eq. (10), it can be deduced that the parallel connected PZ do not con-

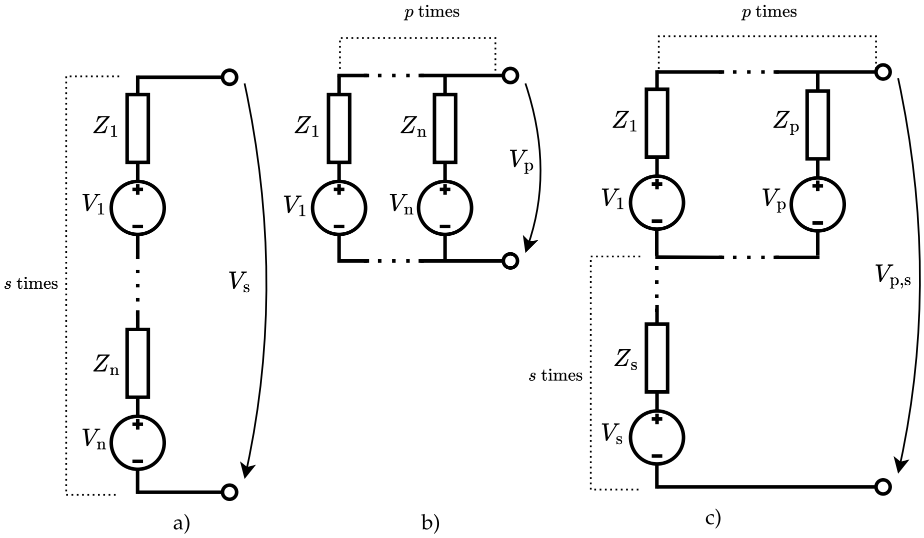

Fig. 10. Combination possibilities with fully Series or Parallel as well as combined architecture of Series and Parallel.

tribute to an increase in the equivalent voltage. In the context of a combined piezoelectric structure operating in both series and parallel configurations, the equivalent model voltages, currents, and impedance are found to be contingent upon the specific nature of the connection structure employed.

For instance, in the case of the PZ associated in series and parallel according to the structure depicted Fig. 10, the equivalent voltage ($V_{\mathrm{p,s}}$) is expressed in Eq. (11), where s and p refer to the number of piezoelectric elements connected in series and parallel, respectively.

$$V_{\mathrm{p,s}} = V_{\mathrm{s}} + V_{\mathrm{p}} = V_0(1+s) \tag{11}$$

The combined equivalent impedance $Z_{\mathrm{p,s}}$ is expressed in Eq. (12). The notation Z_{s} and Z_{p} refer to Eq. (6) and Eq. (9), respectively. It can be seen that the impedance $Z_{\mathrm{p,s}}$ exhibits an increase with rising s, yet remains constant with increasing p.

$$Z_{\mathrm{p,s}} = Z_{\mathrm{s}} + Z_{\mathrm{p}} = \frac{1}{j\omega C}\left(s+\frac{1}{p}\right) \tag{12}$$

According to the delivered equivalent multi of PZ voltage (Eq. (11)) and impedance (Eq. (12)), the load voltage V_{L} is defined based voltage divider rule in Eq. (13).

$$V_{\mathrm{L}} = V_{\mathrm{p,s}} \cdot \frac{R_{\mathrm{L}}}{R_{\mathrm{L}} \cdot Z_{\mathrm{p,s}}} = \frac{(1+s)\cdot R_{\mathrm{L}}}{\frac{1}{j\omega C}(s+\frac{1}{p}) + R_{\mathrm{L}}} V_0 \tag{13}$$

It is evident that the voltage V_{L} is complex; therefore, the product of a complex voltage $\underline{V}$ and a conjugate complex current $\underline{I}^*$ becomes the complex apparent power line.

$$\underline{S} = \underline{V}\cdot\underline{I}^* = \underline{V}\cdot\frac{\underline{V}^*}{R} = \frac{|\underline{V}|^2}{R} \tag{14}$$

In view of the fact that the resistive load is given by $|\underline{S}| = Re\{\underline{S}\} = P_{\mathrm{L}}$ the power is derived to

$$P_L = \frac{V_{\mathrm{L}}^2}{R_{\mathrm{L}}} \tag{15}$$

Substituting equation Eq. (13) into Eq. (15) results in

$$\begin{aligned} P_L &= \left(\frac{V_0(1+s)\ R_{\mathrm{L}}}{\frac{1}{j\omega C}(s+\frac{1}{p}) + R_{\mathrm{L}}}\right)^2 \cdot \frac{1}{R_{\mathrm{L}}} \\ &= \frac{(V_0(1+s))^2 R_{\mathrm{L}}}{(\frac{1}{j\omega C}(s+\frac{1}{p}) + R_{\mathrm{L}})^2} \end{aligned} \tag{16}$$

Table 3
The parameters serve as the foundation for model development.

Parameter	Value
Open Circuit Voltage (V_0)	14 V
Capacitance of PEH (C_{p})	22 nF
Frequency (f_{p})	63 Hz

As shown in Eq. (17), for an optimum load, when the load is equal to the impedance of the piezoelectric arrays, the power is maximised.

$$R_{\mathrm{L}} = |Z_{\mathrm{p,s}}| = \left|\frac{1}{j\omega C}\left(s+\frac{1}{p}\right)\right| \tag{17}$$

This was demonstrated through the derivation of the load power ($\frac{\mathrm{d}P}{\mathrm{d}R_{\mathrm{L}}} = 0$) as expressed in Eq. (18).

$$\frac{\mathrm{d}P_L}{\mathrm{d}R_{\mathrm{L}}} = -\frac{(V_0(1+s))^2(R_{\mathrm{L}} - \frac{1}{\omega C}(s+\frac{1}{p}))}{(\frac{1}{\omega C\ R_{\mathrm{L}}}(s+\frac{1}{p})^3} = 0 \tag{18}$$

The power reaches its maximum when the PEH characteristics are appropriate, and when the number and connection approach match the system load.

$$P_{\max} = \frac{V_{\mathrm{L}}^2}{Z_{\mathrm{p,s}}} = \frac{(V_0(1+s))^2}{4\omega C(s+\frac{1}{p})} \tag{19}$$

4.3. Investigation on multi-piezoelectric element

As shown in Eqs. (13) and (15) to (19) the series and parallel connections influence the equivalent impedance, generated voltage and output power. This effect is illustrated in Fig. 11, which depicts the theoretically generated power, system impedance, and load voltage for various array configurations, ranging from one to ten elements. In this simulation, the model adopted a PEH with the values listed in Table 3.

Fig. 11a illustrates when PZs are connected in parallel, the overall impedance decreases. In contrast, it increases in a pure series connection, as shown in Eq. (12). For devices with internal resistance in the high-impedance range, optimal power output requires at least two PZs connected in series. In contrast, devices with low impedance are better matched with PZ connected in parallel. The increase in voltage with increasing series connections is shown in Fig. 11b. According to Eq. (13),

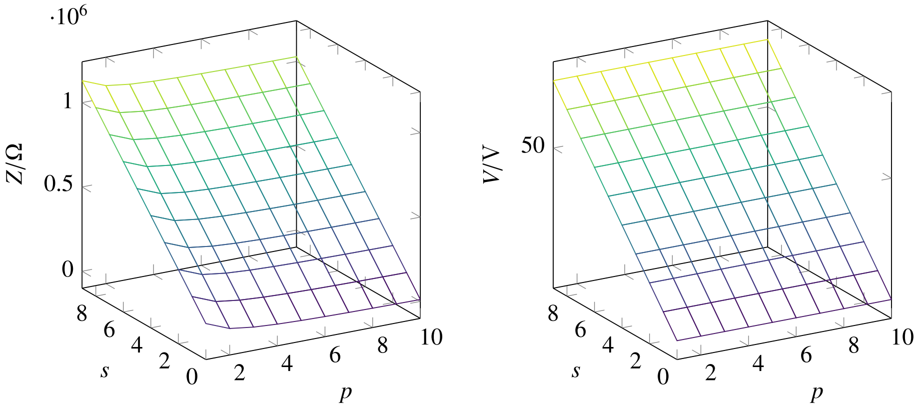

(a) Impedance

(b) Load voltage

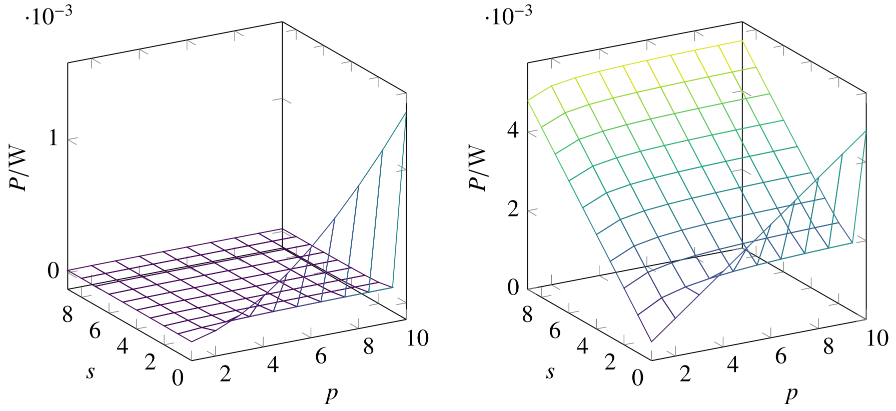

(c) Load power (1 kΩ)

(d) Maximum power

Fig. 11. 3D plots of impedance, voltage load, power load and power maximum.

the voltage increases with an increase in the number of connections, whereas a pure parallel connection does not affect the voltage.

For a 1 kΩ load, the maximum power output generated by the PZs s approximately 1.4 mW of power, as illustrated in Fig. 11c. This maximum power is attained in a purely parallel configuration, which results in lower effective impedance. Conversely, series configurations enable the use of higher load resistances, albeit at the expense of reduced power output. The parallel connection of the PZ array and load maximises the power output when their impedances are matched. Fig. 11d shows that the power of elements in series connection increases significantly, whereas the yield of parallel and series connected elements changes almost insignificantly. Ten PZs in parallel produce an output similar to 15 PZs in series and parallel.

5. Model validation and experimental results

To confirm the relevance and accuracy of the model, laboratory experiments were conducted to validate its theoretical predictions. These results provide a clear basis for evaluating the model's practical feasibility.

5.1. Experimental setup of multi-piezo elements

The analytical model of the MPEH was evaluated and established using the experimental setup shown in Fig. 12a. The PZ is excited using a shaker (TIRA TV 51110), which is powered by a TIRA BAA 120 amplifier and driven by a sine wave generated by an Agilent Technologies 33210A function generator. The frequency and amplitude of the sine wave are adjusted to match the resonance frequency of the transducer, ensuring optimal excitation.

Table 4
Properties of selected PEH.

Parameter	Value
Length (l)	71.0 mm
Width (w)	10.3 mm
Thickness (t)	0.74 mm
Bending mass (m_b)	1.4 g
Capacity (F)	22×10^{-9} F
Piezoelctric Voltage Constant (g_{31})	-9.5×10^{-3} Vm/N
Piezoelectric Charge Constant (d_{31})	-320×10^{-12} m/V

The energy harvesting setup is designed around a cantilever configuration and incorporates up to four MIDE S129-H5FR-1803YB piezoelectric bending transducers. As depicted in Fig. 12b, these transducers are arranged adjacent to and beneath each other. This arrangement enables flexible interconnection of the transducers, allowing them to be linked in parallel or in series depending on the experimental requirements.

Table 4 shows the selected PEH properties, including dimensions and electrical properties. During the system evaluation, the bending beams were actuated at a frequency of 63 Hz and an acceleration of 1 g. This implementation includes ten different array configurations that were investigated experimentally, as shown in Fig. 14. Here, s refers to the number of series elements labelled S, and p refers to the number of parallel elements labelled P. In reality, an energy harvesting system requires at least one PZ is required in an energy harvesting system; therefore, the number of parallel elements starts at 1, as can be seen by looking at Eq. (12), where p cannot become 0. The numbers of connected PZs ranges from 4S, where four PEHs are connected in parallel to 3S1P, where four PEHs are connected in series.

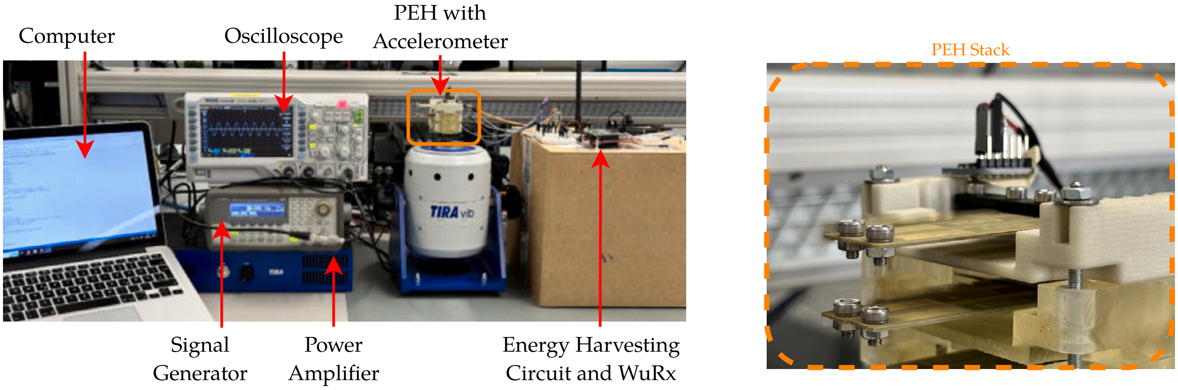

(a) PEH and WuRx setup with used measurement equipment. (b) Detailed view of the PEH stack.

Fig. 12. Experimental setup.

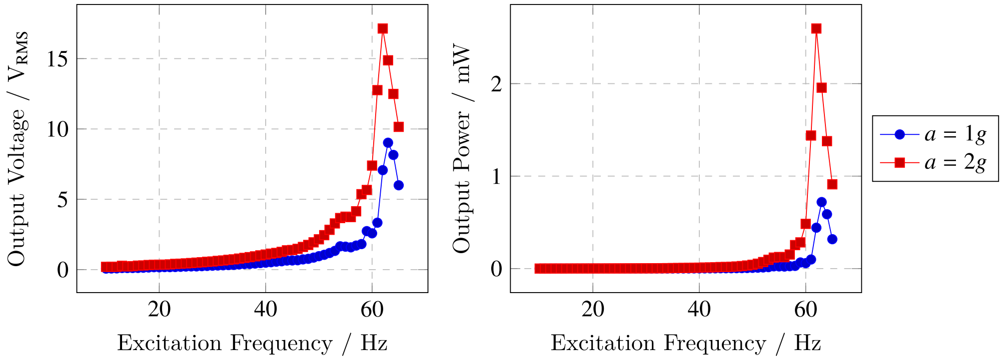

(a) Relationship between voltage and frequency. (b) Relationship between power and frequency.

Fig. 13. Determining the maximum output power with frequency sweep measurement in 0S1P configuration.

5.2. Model validation

To achieve the maximum output power, the resonant frequency of the PEHs was experimentally determined based on the gearbox's frequency range. As previously described, the setup included a frequency generator, an amplifier, a vibration tester, and a PEH in the 0S1P configuration. The proposed PEHs from Mide was tested using a frequency sweep at accelerations of 1 and 2g within a frequency range of 10 to 65 Hz.

The open-circuit voltage was used as the measured output variable. As can be seen in Fig. 13, the peak voltage is observed at 63 Hz, which is the frequency at which the power output is also maximised. This indicates that the resonant frequency f_{res} of the PEH is well matched to the acceleration profile of the gearbox. The resonant frequency can be tuned by adjusting the tip mass [87], in accordance with the relationship [88,89]

$$f_{\mathrm{res}} = f_0 \cdot \sqrt{\frac{m_{\mathrm{b}}}{m_{\mathrm{t}}}} \tag{20}$$

where f_0 denotes the resonant frequency in the absence of a tip mass, m_{b} is the mass of the bending beam, and m_{t} represents the combined mass of the beam and the attached tip mass.

To validate the proposed model, experiments were performed using four identical PZ to derive ten arrays of combinations between series and parallel stages, as illustrated in Fig. 14. To determine the optimal impedance, load sweeps are performed for different array configurations.

The optimum voltage and power for the proposed array variations were investigated through calculations and experiments. Based on Eq. (13), the generated output voltage across a resistance sweep is shown in Figs. 15a, 15c and 15e. As expected, the output voltage remains almost constant with a pure parallel connection. It increases with both variants of the pure series circuit and the mixed circuit. Using the Eq. (19), Figs. 15b, 15d and 15f show the optimum output power of the MPEH with varying resistance.

The power reached a maximum of almost 3 mW for both the pure parallel and pure series connections of the PEH. The optimum load resistance of the 0S4P circuit is approximately 28 kΩ, while of the 3S1P circuit is 450 kΩ. Conceptual modelling of a PEH system usually relies on idealised assumptions, such as optimal material integrity, stable thermal conditions and precisely configured components. However, actual operating environments frequently deviate from these assumptions due to various influencing factors. A correction factor of $c = 0.87$ was introduced to account for these deviations and for mounting in the holder.

Figs. 16a, 16c and 16e show the voltage across the resistance sweep obtained from the experimentalmeasurements. These demonstrate a strong agreement with the calculated curves. The RMS voltages measured at the optimal load for each configuration are shown below: 0S4P – 8.8 V, 3S1P – 33.0 V. Figs. 16b, 16d and 16f display the measured maximum output power across the resistor, including the statistical variation observed in the measurement series. Compared with the calculated values, the maximum power in the 0S4P circuit is 2.85 mW at an optimum resistance of 27 kΩ, while the 3S1P variant delivers 2.6 mW at an optimum resistance of 419 kΩ. Power was calculated using the measured RMS voltage across the known resistive load, according to the formula $P = V_{\mathrm{RMS}}^2/R$.

Measurements were taken using a Rigol DS1054Z oscilloscope with a high-impedance probe, and the waveforms were confirmed to be sinusoidal. This indicates that the pure series circuit deviates from the

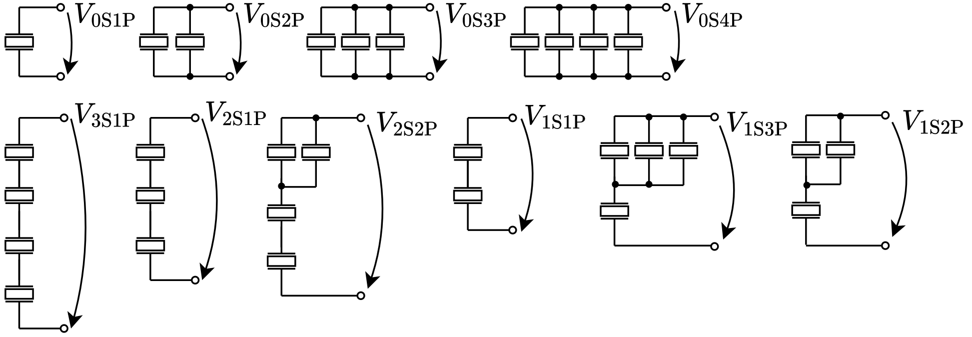

Fig. 14. Ten variants of multi-piezo arrays which are scope of the following investigations.

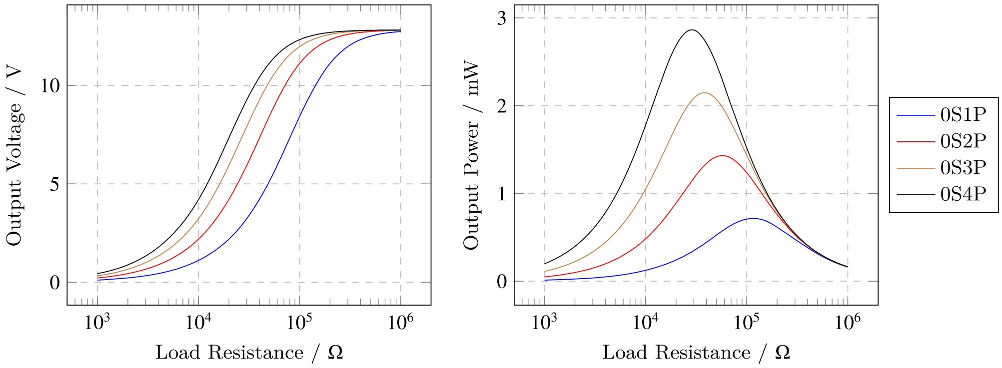

(a) Output voltage of parallel connection.

(b) Output power of parallel connection.

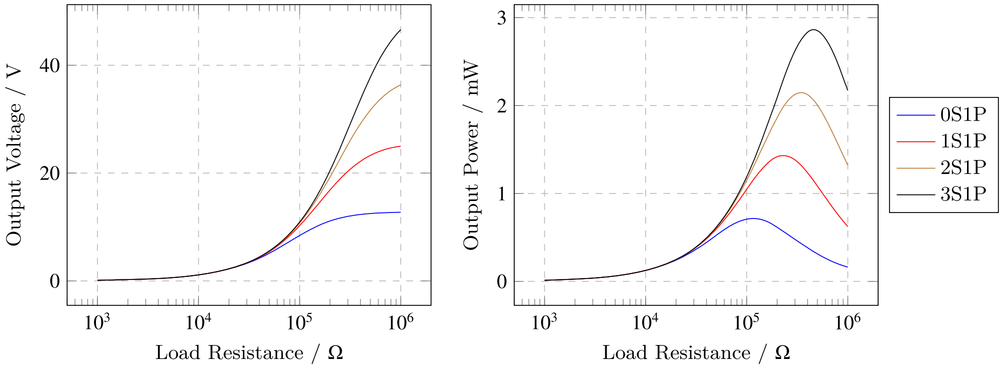

(c) Output voltage of serial connection.

(d) Output power of serial connection.

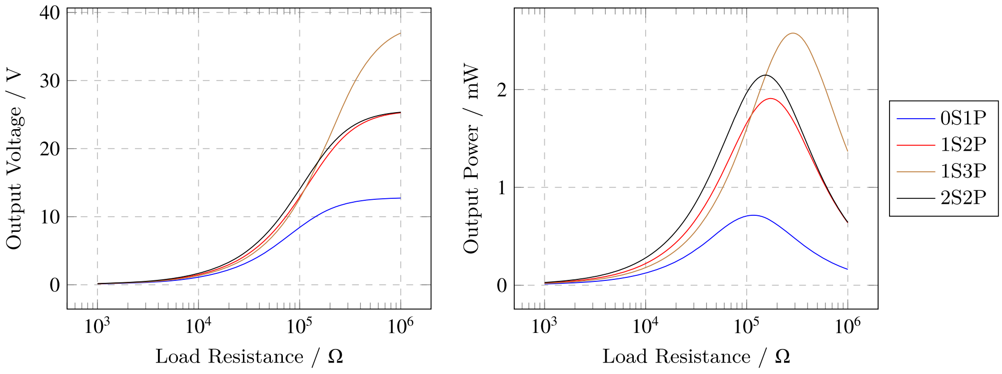

(e) Output voltage of mixed connection.

(f) Output power of mixed connection.

Fig. 15. Calculated AC output values of resistance sweep from proposed model.

theoretical prediction by less than 1 %, whereas the pure parallel configuration exhibits a deviation of approximately 9 %. The measurements exhibit a standard deviation of ± 2 %. Error bars have been omitted from the diagrams to enhance their clarity. Although impedance matching was not explicitly performed, as the focus was on maximum power transfer through resistive sweep, the observed peak power points reflect implicit impedance alignment.

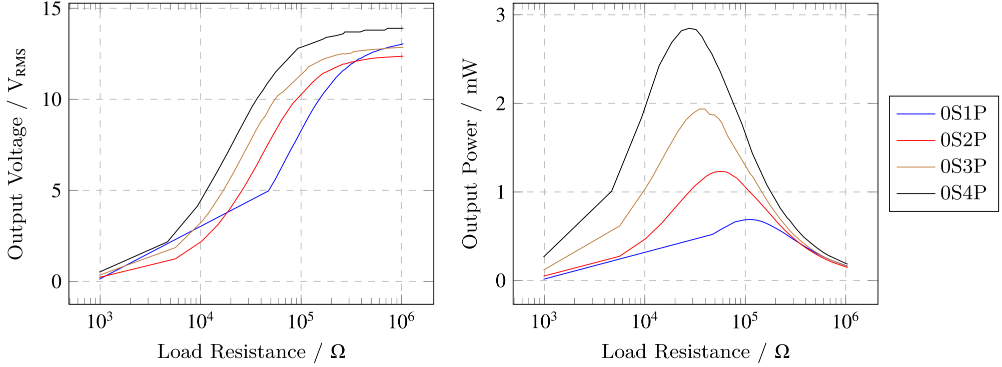

(a) Output voltage of parallel connection.

(b) Output power of parallel connection.

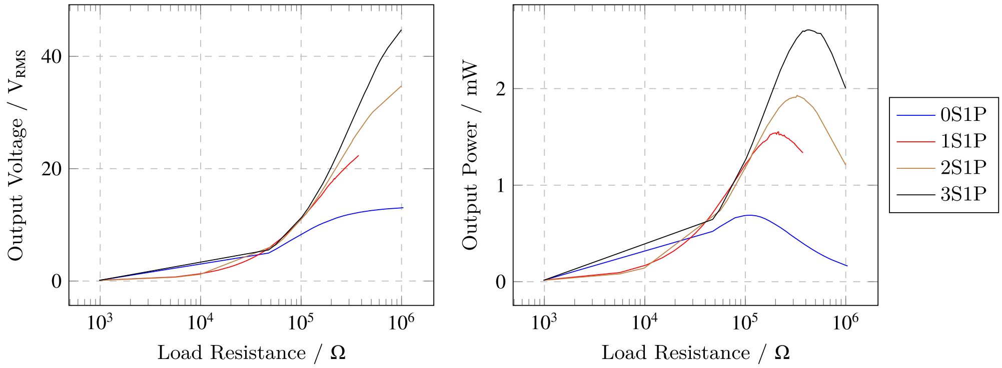

(c) Output voltage of serial connection.

(d) Output power of serial connection.

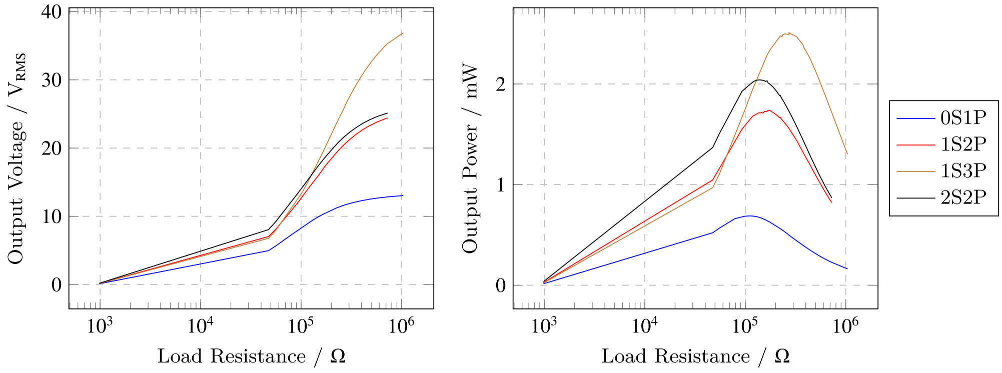

(e) Output voltage of mixed connection.

(f) Output power of mixed connection.

Fig. 16. Experimental AC output values of resistance sweep from PEH.

Table 5 compares the results obtained from the theoretical model with those from the experimental measurements. The optimum impedance, maximum output power, and respective error rates were compared for various piezoelectric arrays. The power results for the 0S2P variant differ by a maximum of 14 % between the theoretical and experimental values. The calculated and measured impedances differ by a maximum of 9 %. These discrepancies highlight the need for further refinement of the theoretical model to better match experimental conditions. In addition, variations in material properties and measurement precision could contribute to these discrepancies. The discrepancies between the theoretical and experimental results are also due to the non-ideal diodes employed for the measurements and the inability to cause the PEH bending beams to oscillate uniformly in terms of both phase and amplitude.

The results show that each array configuration can achieve its peak power within a specific impedance-matching range of the load. In an implementation environment with a device within a certain range of load resistance, adjusting the array variation can increase output power and efficiency. The data show reasonable agreement between theory and experiment, providing a basis for optimising PEH array configurations for practical applications.

Table 5
Error rate of proposed model and validation results.

Array	Model Z_{pzt} (kΩ)	Experiment Z_{pzt} (kΩ)	Error Z_{pzt}	Model P_L (mW)	Experiment P_L (mW)	Error P_L
0S1P	114.8	110.1	4 %	0.72	0.69	4 %
0S2P	57.4	54.5	5 %	1.43	1.23	14 %
0S3P	38.2	34.9	9 %	2.15	1.94	10 %
0S4P	28.7	27.8	3 %	2.86	2.85	1 %
1S1P	229.6	225.6	2 %	1.43	1.53	7 %
1S2P	172.2	168.9	2 %	1.91	1.74	9 %
1S3P	153.1	164.3	7 %	2.15	2.03	5 %
2S1P	344.5	332.8	4 %	2.15	1.92	10 %
2S2P	287.1	272.4	5 %	2.58	2.51	3 %
3S1P	459.3	419.5	9 %	2.86	2.60	9 %

However, the proposed model has certain limitations as it does not account for mechanical factors, environmental conditions, material

Table 6
Power consumption of component values for the wake-up receiver according to working state.

Component	Listening	Detection	Receiving	Transmitting
SPIRIT1	2.8 µW	2.8 µW	29.7 mW	69.3 mW
MSP430 Microcontroller	4.1 µW	4.1 µW	6.6 mW	6.6 mW
AS3933 LF Wake-Up-Receiver IC	10.2 µW	39.6 µW	10.2 µW	10.2 µW
LF Amplifier	4.3 µW	4.3 µW	4.3 µW	4.3 µW
Duration	450 s[1]	26 ms[2]	27 ms[3]	243 ms[4]
Energy	9.6 mJ	1.3 µJ	1 mJ	18.4 mJ

[1] wake-up intervall α.
[2] for 16-bit address.
[3] for 100 byte receiving message.
[4] for 1000 byte data package.

characteristics or mounting precision. The model focuses exclusively on the electrical dynamics of the PEH by design. Consequently, this simplification results in discrepancies between the theoretical predictions and the outcomes observed during experimental validation.

5.3. Energy budget analysis of gearbox monitoring system

The sensor node described in Section 3 requires different energy levels for its various operating states. The device's energy consumption per update period is calculated as follows:

$$E_{\mathrm{WuRx}} = \sum_{i=1}^{N} P_{\mathrm{i}} t_{\mathrm{i}} \tag{21}$$

where E_{WuRx} is the total energy consumed by the node, P_{i} is the power consumption in working mode, t_{i} is the operation period, and N is the maximum power consumption in working mode.

For the operating mode of WuRx, which is illustrated in Fig. 5, there are four working modes ($N = 4$): listening, detection, receiving and transmitting are introduced. In this case, the energy consumption is calculated as

$$E_{\mathrm{WuRx}} = P_{\mathrm{l}} t_{\mathrm{l}} + P_{\mathrm{d}} t_{\mathrm{d}} + P_{\mathrm{r}} t_{\mathrm{r}} + P_{\mathrm{t}} t_{\mathrm{t}} \tag{22}$$

where P_{l}, P_{d}, P_{r} and P_{t} are the power consumption in the listening, detection, receiving, and transmission modes respectively, and t_{l}, t_{d}, t_{r} and t_{t} are the durations of each working mode.

Table 6 presents the detailed power consumption of the individual components within the WuRx across its four primary operational states: listening, detection, receiving, and transmitting. During the listening phase, the WuRx remains idle for an extended period of 450 ms, continuously monitoring for a WuPt while maintaining an ultra-low power draw. The AS3933 LF wake-up receiver IC and the LF amplifier are the dominant contributors to energy consumption in this state, with power requirements of 10.2 µW and the LF amplifier with 4.3 µW respectively, resulting in a total energy consumption of 9.6 mJ.

In the detection state, which lasts only 26 ms, the AS3933 enters a higher-power mode of 39.6 µW to decode the incoming address, while other components remain in a low-power standby configuration. Despite its brief duration, this higher instantaneous power results in an energy cost of 1.3 µJ. Following successful address matching, the receiving state is triggered and lasts 27 ms for a 100-byte message. During this time, the SPIRIT1 transceiver consumes 29.7 mW of power, which contributes significantly to the 1.0 mJ energy expenditure. During the transmission phase, which is required to send a 1000-byte data packet, the SPIRIT1 operates at 69.3 mW for 243 ms, resulting in the highest per-event energy cost of 18.4 mJ.

This energy profile is used to capture the relationship between listening and communication duration and total energy consumption. This forms the basis for deriving the battery lifetime by quantifying energy usage across all operational phases.

$$T_{\mathrm{WuRx}} = t_{\mathrm{l}} + t_{\mathrm{d}} + t_{\mathrm{r}} + t_{\mathrm{t}} \tag{23}$$

The number N of communication update a node can perform during its entire battery's lifetime is

$$N = \frac{E_{\mathrm{Bat}}}{E_{\mathrm{WuRx}}} \tag{24}$$

with E_{Bat} being the battery's lifetime initial energy. The duration of the battery life t_{Bat} can be determined using the following equation

$$t_{\mathrm{bat}} = N \cdot T_{\mathrm{WuRx}} \cdot \frac{1}{3600} \frac{1}{24} \frac{1}{365} \tag{25}$$

Based on Eqs. (22) to (25) and the parameter values presented in Table 6, assuming a 1100 mAh 2/3 AA-format battery powers the sensor node, the estimated battery lifetime t_{Bat} is approximately 6.5 years.

Under a realistic operational duty cycle involving a communication event every 450.3 s, comprising 450 s in passive listening mode followed by 300 ms of active engagement encompassing detection, reception, and transmission, the total energy expenditure per cycle is approximately 29 mJ, as presented in Table 6. This results in an average power demand of 64.4 µW. Since the PEH provides a continuous output of 2.86 mW, it substantially exceeds the system's average power requirement. However, since transient peak power demands of up to 75 mW are incurred during the active phase, an energy storage device is necessary to buffer these short-duration loads and ensure uninterrupted power delivery. Supercapacitors are well suited to this purpose as they can discharge rapidly to accommodate high instantaneous power demands and recharge during the low-power listening phase. Furthermore, they operate on direct current, which corresponds to the voltage requirements of the sensor node's components.

The electrical output of the PEH is an AC voltage by nature, which requires conversion to a DC voltage to ensure compatibility with the sensor node and the energy storage components. This conversion is usually achieved by integrating power management circuitry that incorporates the appropriate DC-DC converters. Several commercially available converters are suitable for this application, such as the LTC3129, AEM30940-QFN, LTC3588-1, and TPS62125. These devices facilitate efficient energy transfer and voltage regulation, thereby supporting the continuous and reliable operation of the Wake-up Receiver under the defined duty cycle, even in the presence of power management overhead. The LTC3588-1 is selected for its high efficiency of around 90 % and its wide operating range, which can achieve an input voltage of up to 20 V. While the WuRx is supplied by the MPEH, an energy management circuit is required to charge the supercapacitor while the system is operating.

The harvested energy can be stored in the input capacitor. The wide voltage input range takes advantage of the fact that energy stored in a capacitor is proportional to the square of its voltage. Furthermore, this AC-DC converter incorporates a rectifier stage, making it a compact solution. The rectifier and buck converter provide a constant output voltage of 3.3 V meaning that the microcontroller of the sensor node is not exposed to fluctuating voltages.

Fig. 17 illustrates the schematic structure of the test setup. The MPEH is connected to PZ1 and PZ2 of the LTC3588, and a 3 mF capacitor is connected to V_{IN}, the size of which is determined by Eq. (26) and the values from Table 6.

$$C = \frac{2 \cdot E}{V^2} \tag{26}$$

A small smoothing capacitor C_{OUT} with a capacitance of 100 µF is connected to the output along with WuRx as the load. A transmitter node sends a WuPt signal and a data packet to the WuRx to request sensor data. The WuRx receives the WuPt, decodes it and retrieves the data for querying data. It then transmits the required measurement data back to the transmitter node.

Fig. 18 shows the voltage of the supercapacitor and the load current of the sensor node. The capacitor compensates for load peaks and

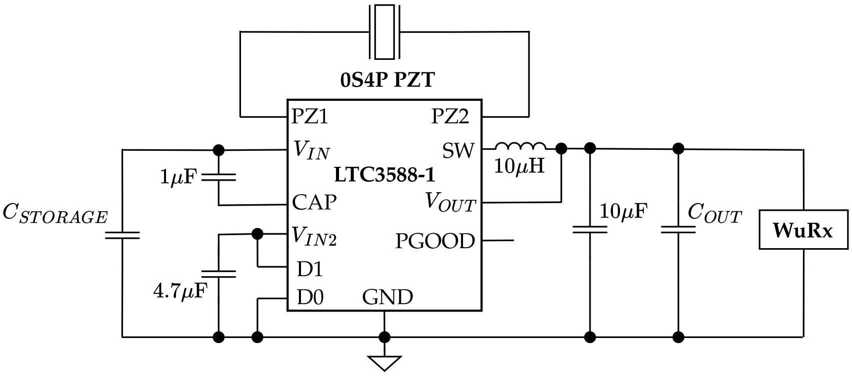

Fig. 17. Block Diagram of the Energy Harvesting Module Utilizing the LTC3588-1.

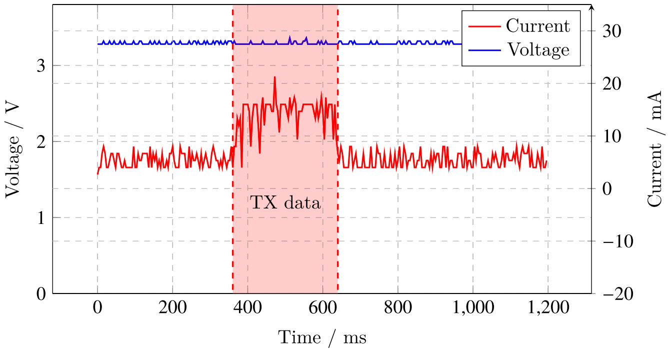

Fig. 18. Supercap is supplying WuRx node.

maintains an uninterrupted power supply. Most of the required energy is consumed by communication between the sensor nodes. For a data size of 920 Byte, the transmitted and received currents can peak at 20 mA for up to 240 ms. The evaluation showed that the voltage remained stable despite the high current demand. The capacitor buffers the energy required for active communication between the sensor nodes. In this case, the number of PEH can be designed according to application-specific power requirements, as well as existing frequency and acceleration levels.

6. Discussion

This study introduces a modelling framework for evaluating the power output in MPEH circuits, with focus on impedance matching between the PEH and a resistive load. The proposed approach eliminates the need for matching networks, supporting autonomous energy delivery to ultra-low-power electronic systems. This is particularly advantageous for maintenance-free deployments in industrial monitoring scenarios.

Experimental validation was performed using a sensor node equipped with a WuRx, which was selected for its passive front end and asynchronous communication architecture, both of which significantly reduce power consumption relative to traditional sensor platforms. To evaluate the model under application-relevant conditions, vibration-based energy harvesting was explored using gearbox excitation profiles. The mechanical energy, which was emulated using laboratory-controlled inputs, was transduced by the PEH to power the WuRx sensor node.

This work is a proof-of-concept study based on controlled laboratory experiments conducted using a TIRA vibration shaker system. While no field tests were conducted on an actual gearbox, the experimental excitation conditions were derived from real-world vibration profiles provided by the system operator. This ensures the testing environment is both practical and realistic.

The resonance frequencies of both the PEH and the emulated gearbox structure were determined, enabling precise alignment of the harvester impedance characteristics with the WuRx power demands. Theoretical predictions were validated by experimental outcomes, demonstrating that the WuRxnode, which requires approximately 29 mJ per monitoring cycle, can be reliably powered using harvested vibration energy. Peak transmission loads of up to 75 mW were effectively buffered using a 3 mF supercapacitor, enabling stable, repeatable operation.

These results demonstrate the feasibility of implementing energy-autonomous WS systems in vibration-rich environments, with significant implications for deployment in hard-to-access industrial machinery. Although the research was conducted in a laboratory setting, the findings confirm that the energy requirements of WuRx-enabled nodes can be met using MPEH designs under realistic excitation conditions. Efficiency could be further enhanced by optimising the voltage converter circuit, which currently assumes a constant excitation frequency. Incorporating variable-frequency behaviour in future iterations would improve the system's adaptability and resilience. Furthermore, significant performance improvements can be achieved through targeted circuit refinement, despite the use of commercially available components.

In terms of configuration, parallel PEH architectures are recommended when the excitation is non-uniform or asynchronous, as is often observed in rotating or industrial equipment. These setups ensure consistent voltage output and fault-tolerant energy contribution from individual elements. Conversely, series configurations are suitable for applications requiring synchronised excitation and high-voltage output, albeit under more controlled or structured conditions. The choice between these configurations should be based on the expected vibration profile and energy management requirements of the target application.

7. Conclusion

The experimental findings unequivocally demonstrate that the 4P (0S4P) configuration offers the most effective trade-off between impedance level and energy delivery for short-duration, high-current discharges, which are essential for data transmission in WuRx-based sensor nodes. Peak power levels of up to 75 mW were successfully managed through the utilisation of a 3 mF supercapacitor in conjunction with the LTC3588-1 energy management module. The findings emphasise that the deliberate selection of the PZ configuration can significantly enhance the reliability of event-driven sensor operations in demanding environments, such as gearbox condition monitoring applications. Furthermore, the present study corroborates the viability of vibration-based energy harvesting for powering gearbox monitoring systems utilising a PEH-powered WuRx sensor node.

The experimental validation closely aligns with the theoretical model, thereby establishing that the harvested energy is sufficient to meet the operational demands of the WuRx sensor. This approach facilitates the development of energy-autonomous wireless sensors for deployment in inaccessible or hazardous locations. It is recommended that future research efforts concentrate on the optimisation of the voltage converter circuitry with a view to enhancing the overall efficiency of PEH systems. The incorporation of variable frequency operation in subsequent designs has the potential to enhance the adaptability and resilience of the system in dynamic environmental conditions. Despite the reliance on commercially available components, significant performance improvements are possible through careful circuit-level improvements.

- The selection of PZ configuration has been demonstrated to directly enhance the reliability of WuRx-based event-driven sensors in harsh environments. The 4P (0S4P) configuration has been demonstrated to provide an optimal balance between impedance and energy output for brief, high-current bursts.
- It has been demonstrated that power peaks of up to 75 mW can be effectively managed by utilising a 3 mF supercapacitor in conjunction with the LTC3588-1 module. Vibration-based energy harvesting has been identified as a viable method for powering gearbox monitoring systems.
- Theoretical models were subjected to experimental validation, thereby confirming the sufficiency of harvested energy for the operation of the WuRx sensor.
- Future research should concentrate on voltage converters and the integration of variable-frequency control to enhance efficiency, adaptability, and performance using standard components.

CRediT authorship contribution statement

Lydia Schott: Writing – review & editing, Writing – original draft, Visualization, Validation, Software, Methodology, Investigation, Funding acquisition, Data curation, Conceptualization. **Ghada Bouattour:** Writing – review & editing, Writing – original draft, Formal analysis, Conceptualization. **Robert Fromm:** Writing – review & editing, Writing – original draft, Methodology, Formal analysis. **Florian Strakosch:** Data curation. **Olfa Kanoun:** Writing – review & editing, Supervision. **Faouzi Derbel:** Writing – review & editing, Supervision.

Funding

This research was funded by the European Union Social Fund (grant number K-7531.20/496-11 and financially supported by the Leipzig University of Applied Sciences with funds from the Sächsisches Staatsministerium für Wissenschaft, Kultur und Tourismus.

Declaration of competing interest

The authors declare that they have no known competing financial interests or personal relationships that could have appeared to influence the work reported in this paper.

Data availability

Data will be made available on request.

References

[1] S. Khriji, D.E. Houssaini, I. Kammoun, K. Besbes, O. Kanoun, Energy-efficient routing algorithm based on localization and clustering techniques for agricultural applications, IEEE Aerosp. Electron. Syst. Mag. 34 (3) (2019) 56–66, https://doi.org/10.1109/MAES.2019.2905947.

[2] E.F. Da Costa, N.E. de Oliveira, F.J.O. Morais, P. Carvalhaes-Dias, L.F.C. Duarte, A. Cabot, J.A. Siqueira Dias, A self-powered and autonomous fringing field capacitive sensor integrated into a micro sprinkler spinner to measure soil water content, Sensors 17 (3) (2017) 575, https://doi.org/10.3390/s17030575.

[3] N. Sushma, H.N. Suresh, L.J. Mohana, K.B. Santhosh Kumar, Experimental investigation on wireless integrated smart system for energy and water resource management in Indian smart cities, Results Eng. 23 (2024) 102687, https://doi.org/10.1016/j.rineng.2024.102687.

[4] M.K. Baazaoui, I. Ketata, G. Fersi, A. Fakhfakh, F. Derbel, Implementation of rssi module in omnet++ for investigation of wsn simulations based on real environmental conditions, in: Proceedings of the 11th International Conference on Sensor Networks - EWSN-IoT, INSTICC, SciTePress, 2022, pp. 281–287.

[5] I. Ahmad, A.M. Tosif, Alina Abdelrhman, S. Chithambaram, S.A. Imam, M. Hammad, Design development and testing of traffic induced wind based artificial tree type hybrid energy harvester for wireless sensor nodes, Results Eng. 20 (2023) 101515, https://doi.org/10.1016/j.rineng.2023.101515.

[6] S.H. Khasteh, H. Rokhsati, On transmission range of sensors in sparse wireless sensor networks, Results Eng. 18 (2023) 101108, https://doi.org/10.1016/j.rineng.2023.101108.

[7] L. Schott, F. Strakosch, F. Derbel, Validation of energy harvesting designs for autarkic wireless sensor networks, in: 16th IEEE International Multi-Conference on Systems, Signals and Devices (SSD'19), IEEE, Piscataway, NJ, 2019, pp. 328–333.

[8] G. Bouattour, M. Elhawy, S. Naifar, C. Viehweger, H. Ben Jmaa Derbel, O. Kanoun, Multiplexed supply of a miso wireless power transfer system for battery-free wireless sensors, Energies 13 (5) (2020) 1244, https://doi.org/10.3390/en13051244.

[9] L.-T. Huang, J.-Y. Chang, Vibration characterization and fault diagnosis of a planetary gearbox with a wireless embedded sensor, Appl. Sci. 13 (2) (2023) 729, https://doi.org/10.3390/app13020729.

[10] F. Derbel, F. Strakosch, Integrated sensor based smart diagnostic and online monitoring of industrial systems, in: 2022 4th International Conference on Applied Automation and Industrial Diagnostics (ICAAID 2022), Institute of Electrical and Electronics Engineers (IEEE), Piscataway, NJ, USA, 2022, pp. 1–6.

[11] O. Kanoun, S. Khriji, S. Naifar, S. Bradai, G. Bouattour, A. Bouhamed, D. El Houssaini, C. Viehweger, Prospects of wireless energy-aware sensors for smart factories in the industry 4.0 era, Electronics 10 (23) (2021) 2929, https://doi.org/10.3390/electronics10232929.

[12] G. Peruzzi, A. Pozzebon, A review of energy harvesting techniques for low power wide area networks (lpwans), Energies 13 (13) (2020) 3433, https://doi.org/10.3390/en13133433.

[13] R.I. Pereira, S.C. Jucá, P.C. Carvalho, Iot embedded systems network and sensors signal conditioning applied to decentralized photovoltaic plants, Measurement 142 (2019) 195–212, https://doi.org/10.1016/j.measurement.2019.04.085.

[14] I. Korhonen, R. Lankinen, Energy harvester for a wireless sensor in a boiler environment, Measurement 58 (2014) 241–248, https://doi.org/10.1016/j.measurement.2014.08.037.

[15] T. Keutel, T. Motl, S. Bdiri, C. Viehweger, O. Kanoun, Robust power supply for wireless sensors using the electrostatic field of parts under high voltage, in: 2012 International Conference on Smart Grid Technology, Economics and Policies (SG-TEP), 2012, pp. 1–4.

[16] S. Bradai, S. Naifar, C. Viehweger, O. Kanoun, E. Manoach, S. Stoykov, M. Wiercigroch, Electromagnetic vibration energy harvesting for railway applications, MATEC Web Conf. 148 (8) (2018) 12004, https://doi.org/10.1051/matecconf/201814812004.

[17] F. Giusa, F. Maiorca, A. Noto, C. Trigona, B. Andò, S. Baglio, A diode-less mechanical voltage multiplier: a novel transducer for vibration energy harvesting, Sens. Actuators A, Phys. 212 (2014) 34–41, https://doi.org/10.1016/j.sna.2014.03.017.

[18] H.W. Kim, A. Batra, S. Priya, K. Uchino, D. Markley, R.E. Newnham, H.F. Hofmann, Energy harvesting using a piezoelectric "cymbal" transducer in dynamic environment, Jpn. J. Appl. Phys. 43 (9R) (2004) 6178, https://doi.org/10.1143/JJAP.43.6178.

[19] O. Kanoun, S. Bradai, S. Khriji, G. Bouattour, D. El Houssaini, M. Ben Ammar, S. Naifar, A. Bouhamed, F. Derbel, C. Viehweger, Energy-aware system design for autonomous wireless sensor nodes: a comprehensive review, Sensors 21 (2) (2021) 548, https://doi.org/10.3390/s21020548.

[20] R. Caliò, U.B. Rongala, D. Camboni, M. Milazzo, C. Stefanini, G. de Petris, C.M. Oddo, Piezoelectric energy harvesting solutions, Sensors 14 (3) (2014) 4755–4790, https://doi.org/10.3390/s140304755.

[21] J. Ding, M. Lu, A. Deng, S. Jiang, A piezoelectric energy harvester using an arc-shaped piezoelectric cantilever beam array, Microsyst. Technol. 28 (8) (2022) 1947–1958, https://doi.org/10.1007/s00542-022-05338-0.

[22] R. Elfrink, M. Renaud, T.M. Kamel, C. de Nooijer, M. Jambunathan, M. Goedbloed, D. Hohlfeld, S. Matova, V. Pop, L. Caballero, R. van Schaijk, Vacuum-packaged piezoelectric vibration energy harvesters: damping contributions and autonomy for a wireless sensor system, J. Micromech. Microeng. 20 (10) (2010) 0, https://doi.org/10.1088/0960-1317/20/10/104001.

[23] H. Kim, S. Priya, K. Uchino, Modeling of piezoelectric energy harvesting using cymbal transducers, Jpn. J. Appl. Phys. 45 (7) (2006) 5836–5840, https://doi.org/10.1143/JJAP.45.5836.

[24] G. Lombardi, M. Lallart, M. Kiziroglou, E.M. Yeatman, A piezoelectric self-powered active interface for ac/dc power conversion improvement of electromagnetic energy harvesting, Smart Mater. Struct. 29 (11) (2020) 117002, https://doi.org/10.1088/1361-665X/abadd3.

[25] M. Ferrari, V. Ferrari, M. Guizzetti, B. Andò, S. Baglio, C. Trigona, Improved energy harvesting from wideband vibrations by nonlinear piezoelectric converters, Sens. Actuators A, Phys. 162 (2) (2010) 425–431, https://doi.org/10.1016/j.sna.2010.05.022.

[26] Q. Tang, Q. He, M. Li, C. Dong, D. Xu, X. Li, Wireless alarm microsystem self-powered by vibration-threshold triggered energy-harvester, IEEE Trans. Ind. Electron. 63 (4) (2015) 1, https://doi.org/10.1109/TIE.2015.2510503.

[27] J. Kymissis, C. Kendall, J. Paradiso, N. Gershenfeld, Parasitic power harvesting in shoes, in: Second International Symposium on Wearable Computers, IEEE Computer Society Press, Los Alamitos, Calif, 2010, pp. 132–139.

[28] F. Dell'Anna, T. Dong, P. Li, Y. Wen, Z. Yang, M.R. Casu, M. Azadmehr, Y. Berg, State-of-the-art power management circuits for piezoelectric energy harvesters, IEEE Circuits Syst. Mag. 18 (3) (2018) 27–48, https://doi.org/10.1109/MCAS.2018.2849262.

[29] M. Ben Ammar, S. Sahnoun, A. Fakhfakh, C. Viehweger, O. Kanoun, Self-powered synchronized switching interface circuit for piezoelectric footstep energy harvesting, Sensors 23 (4) (2023) 1830, https://doi.org/10.3390/s23041830.

[30] A. Elgani, M. Magno, F. Renzini, L. Perilli, E.F. Scarselli, A. Gnudi, R. Canegallo, G. Ricotti, L. Benini, Nanowatt wake-up radios: discrete-components and integrated architectures, in: ICECS, Institute of Electrical and Electronics Engineers, Piscataway, New Jersey, 2018, pp. 793–796.

[31] M. Vodel, M. Caspar, W. Hardt, Wake-up-receiver concepts - capabilities and limitations, J. Netw. 7 (2012) 126–134, https://doi.org/10.4304/jnw.7.1.126-134.

[32] C.A. Fumtchum, F.D. Hutu, P. Tsafack, G. Villemaud, E. Tanyi, Towards a battery-free wake-up radio, Electronics 10 (20) (2021) 2449, https://doi.org/10.3390/electronics10202449.

[33] A.M. Graham, S.D. Asimonis, Practical superdirective and efficient rectenna for low-power rf energy harvesting, in: 2024 IEEE-APS Topical Conference on Antennas and Propagation in Wireless Communications (APWC), IEEE, Piscataway, NJ, 2024, pp. 188–191.

[34] R. Fromm, O. Kanoun, F. Derbel, An improved wake-up receiver based on the optimization of low-frequency pattern matchers, Sensors 23 (19) (2023) 8188, https://doi.org/10.3390/s23198188.

[35] N. Panayanthatta, G. Clementi, M. Ouhabaz, M. Costanza, S. Margueron, A. Bartasyte, S. Basrour, E. Bano, L. Montes, C. Dehollain, R. La Rosa, A self-powered and battery-free vibrational energy to time converter for wireless vibration monitoring, Sensors 21 (22) (2021) 7503, https://doi.org/10.3390/s21227503.

[36] L. Wang, T. He, Z. Zhang, L. Zhao, C. Lee, G. Luo, Q. Mao, P. Yang, Q. Lin, X. Li, R. Maeda, Z. Jiang, Self-sustained autonomous wireless sensing based on a hybridized teng and peg vibration mechanism, Nano Energy 80 (2021) 105555, https://doi.org/10.1016/j.nanoen.2020.105555.

[37] B. Zhang, D. Li, Y. Li, B. Ducharne, J. Gao, Double peak derived from piezoelectric coefficient nonlinearity and proposal for self-powered systems, Trans. Nanjing Univ. Aeronaut. Astronaut. 35 (1) (2018) 109–115, https://doi.org/10.16356/j.1005-1120.2018.01.109.

[38] Y. Ma, Q. Ji, S. Chen, G. Song, An experimental study of ultra-low power wireless sensor-based autonomous energy harvesting system, J. Renew. Sustain. Energy 9 (5) (2017) 054702, https://doi.org/10.1063/1.4997274.

[39] V. Ostasevicius, V. Markevicius, V. Jurenas, M. Zilys, M. Cepenas, L. Kizauskiene, V. Gyliene, Cutting tool vibration energy harvesting for wireless sensors applications, Sens. Actuators A, Phys. 233 (2015) 310–318, https://doi.org/10.1016/j.sna.2015.07.014.

[40] J. Lee, B. Choi, Development of a piezoelectric energy harvesting system for implementing wireless sensors on the tires, Energy Convers. Manag. 78 (2014) 32–38, https://doi.org/10.1016/j.enconman.2013.09.054.

[41] N.S. Shenck, J.A. Paradiso, Energy scavenging with shoe-mounted piezoelectrics, IEEE MICRO 21 (3) (2001) 30–42, https://doi.org/10.1109/40.928763.

[42] M. Atif Shahzad, S. Sahmani, B. Safaei, Nonlocal couple stress-based meshless collocation model for nonlinear dynamic performance of microbeam-type piezoelectric energy harvesters, Eur. J. Mech. A Solids 101 (2023) 105059, https://doi.org/10.1016/j.euromechsol.2023.105059.

[43] R. Alshenawy, S. Sahmani, B. Safaei, Y. Elmoghazy, A. Al-Alwan, M.A. Nuwairan, Three-dimensional nonlinear stability analysis of axial-thermal-electrical loaded fg piezoelectric microshells via mkm strain gradient formulations, Appl. Math. Comput. 439 (2023) 127623, https://doi.org/10.1016/j.amc.2022.127623.

[44] P. Milić, D. Marinković, S. Klinge, Ž. Ćojbašić, Reissner-Mindlin based isogeometric finite element formulation for piezoelectric active laminated shells, Teh. Vjesn. - Stroj. Fak. 30 (2) (2023), https://doi.org/10.17559/TV-20230128000280.

[45] A. Tabak, B. Safaei, A. Memarzadeh, S. Arman, C. Kizilors, An extensive review of piezoelectric energy-harvesting structures utilizing auxetic materials, J. Vib. Eng. Technol. 12 (3) (2024) 3155–3192, https://doi.org/10.1007/s42417-023-01038-9.

[46] L. Li, P. Deng, Y. Fan, Dynamic characteristics of a cyclic-periodic structure with a piezoelectric network, Chin. J. Aeronaut. 28 (5) (2015) 1426–1437, https://doi.org/10.1016/j.cja.2015.08.014.

[47] M. Hunstig, W. Al-Ashtari, T. Hemsel, W. Sextro, Leistungs- und bandbreitensteigerung von energy-harvesting-generatoren für energieautarke systeme, in: 9. Paderborner Workshop Entwurf Mechatronischer Systeme Paderborn, Verlagsschriftenreihe des Heinz Nixdorf Instituts, Paderborn, Verlagsschriftenreihe des Heinz Nixdorf Instituts, Paderborn, Paderborn, 2013, pp. 1–14, https://api.semanticscholar.org/CorpusID:112189592.

[48] S. Du, Y. Jia, A.A. Seshia, Piezoelectric vibration energy harvesting: a connection configuration scheme to increase operational range and output power, J. Intell. Mater. Syst. Struct. 28 (14) (2017) 1905–1915, https://doi.org/10.1177/1045389X16682846.

[49] M. Meng, D. Wang, B.D. Truong, S. Trolier-McKinstry, S. Roundy, M. Kiani, A multi-beam shared-inductor reconfigurable voltage/sece mode piezoelectric energy harvesting interface circuit, IEEE Trans. Biomed. Circuits Syst. 13 (6) (2019) 1277–1287, https://doi.org/10.1109/TBCAS.2019.2942261.

[50] S.Y. Jeong, J.Y. Cho, S.D. Hong, W. Hwang, H. Jabbar, J.H. Ahn, J.P. Jhun, T.H. Sung, Self-powered operational amplifying system with a bipolar voltage generator using a piezoelectric energy harvester, Electronics 9 (1) (2020) 1–11, https://doi.org/10.3390/electronics9010041.

[51] N.A. Abidin, N.M. Nayan, M. Azizan, N. Jamel, A. Ali, N. Azli, N. Nordin, Performances of multi-configuration piezoelectric connection with ac-dc converter in low frequency energy harvesting system, J. Phys. Conf. Ser. 2550 (1) (2023) 012001, https://doi.org/10.1088/1742-6596/2550/1/012001.

[52] Z. Li, Z. Chen, Q. Wan, Q. Kuai, J. Liang, P. Mok, X. Zeng, An energy harvesting system with reconfigurable piezoelectric energy harvester array for iot applications, in: 2020 IEEE International Symposium on Circuits and Systems (ISCAS), 2020, pp. 1–5.

[53] U. Aridogan, I. Basdogan, A. Erturk, Multiple patch–based broadband piezoelectric energy harvesting on plate-based structures, J. Intell. Mater. Syst. Struct. 25 (14) (2014) 1664–1680, https://doi.org/10.1177/1045389X14544152.

[54] A. Aghakhani, I. Basdogan, A. Erturk, Multiple piezo-patch energy harvesters integrated to a thin plate with ac-dc conversion: analytical modeling and numerical validation, in: N.G. Meyendorf, T.E. Matikas, K.J. Peters (Eds.), Smart Materials and Nondestructive Evaluation for Energy Systems 2016, in: SPIE Proceedings, SPIE, 2016, p. 98060C.

[55] L. Mateu, L. Lühmann, H. Zessin, P. Spies, Modified parallel sshi ac-dc converter for piezoelectric energy harvesting power supplies, in: 2011 IEEE 33rd International Telecommunications Energy Conference (INTELEC), 2011, pp. 1–7.

[56] J. Brufau-Penella, M. Puig-Vidal, Piezoelectric energy harvesting improvement with complex conjugate impedance matching, J. Intell. Mater. Syst. Struct. 20 (5) (2009) 597–608, https://doi.org/10.1177/1045389X08096051.

[57] S. Bradai, C. Trigona, S. Naifar, S. Baglio, O. Kanoun, Rmshi solutions for electromagnetic transducers from environmental vibration, in: B. Andò, F. Baldini, C. Di Natale, V. Ferrari, V. Marletta, G. Marrazza, V. Militello, G. Miolo, M. Rossi, L. Scalise, P. Siciliano (Eds.), Sensors, SpringerLink Bücher, Springer International Publishing, Cham, 2019, pp. 599–607.

[58] N.A. Abidin, N.M. Nayan, M. Azizan, A. Ali, N. Hussin, N.A. Azli, N.M. Nordin, The simulation analysis of piezoelectric transducer with multi-array configuration, J. Phys. Conf. Ser. 1432 (2020) 012042, https://doi.org/10.1088/1742-6596/1432/1/012042.

[59] L.H. Fang, R.b.A. Rahim, M.I.F. Romli, M.Z. Zakariya, J.B.A.M. Jobran, N.B. Kimpol, Piezoelectric array configuration technique into enhance power catchment for sound energy harvester system, in: 2020 International Conference on Sustainable Energy Engineering and Application (ICSEEA), 2020, pp. 1–9.

[60] M.S. Khan, N. Sultana, M.A. Himel, Foot step power generation: a comparative analysis of multi-array piezoelectric transducer configurations, in: 2023 6th International Conference on Electrical Information and Communication Technology (EICT), IEEE, Piscataway, NJ, 2023, pp. 1–6.

[61] M.S. Morshed, T. Imam Sourav, M.H. Maruf, A. Al Mansur, R.H. Ashique, L. Nima, A thorough probe into enhancing energy harvesting via piezo-modules in metrorail stations, in: 2023 10th IEEE International Conference on Power Systems (ICPS), IEEE, Piscataway, NJ, 2023, pp. 1–4.

[62] M. Moreno, J.A. Morales-Viscaya, M.X. Cuevas-Gayosso, J.G. Parada-Salado, F.J. Perez-Pinal, Optimized equivalent circuit models for series-parallel configurations of piezoelectric transducers in energy harvesting, PLoS ONE 20 (6) (2025) e0323682, https://doi.org/10.1371/journal.pone.0323682.

[63] G. Wang, R. Song, L. Luo, P. Yu, X. Yang, L. Zhang, Multi-piezoelectric energy harvesters array based on wind-induced vibration: design, simulation, and experimental evaluation, Energy 300 (2024) 131509, https://doi.org/10.1016/j.energy.2024.131509.

[64] S. Bouhedma, J. Bin Taufik, F. Lange, M. Ouali, H. Seitz, D. Hohlfeld, Different scenarios of autonomous operation of an environmental sensor node using a piezoelectric-vibration-based energy harvester, Sensors 24 (4) (2024) 1338, https://doi.org/10.3390/s24041338.

[65] L. Chen, M. Zhang, Z. Xu, H. Chen, J. Xu, A multiple-cantilever piezoelectric vibration energy harvester for self-powered co2 monitoring in transformer substations, Appl. Sci. 14 (23) (2024) 10805, https://doi.org/10.3390/app142310805.

[66] F. Rigo, M. Migliorini, A. Pozzebon, Piezoelectric sensors as energy harvesters for ultra low-power iot applications, Sensors 24 (8) (2024), https://doi.org/10.3390/s24082587.

[67] L. Wang, L. Zhao, G. Luo, Y. Zhao, P. Yang, Z. Jiang, R. Maeda, System level design of wireless sensor node powered by piezoelectric vibration energy harvesting, Sens. Actuators A, Phys. 310 (2020) 112039, https://doi.org/10.1016/j.sna.2020.112039.

[68] K. Singh, P. Shukla, S.S. M, N.K. Gnani, P.T. V, J. Kuri, Judicious data management for sustaining an energy harvesting sensor node, Concurr. Comput. Pract. Exp. (2020) e5997, https://doi.org/10.1002/cpe.5997.

[69] F. Wang, M. Zhou, P. Wu, L. Gao, X. Chen, X. Mu, Self-powered transformer intelligent wireless temperature monitoring system based on an ultra-low acceleration piezoelectric vibration energy harvester, Nano Energy 114 (2023) 108662, https://doi.org/10.1016/j.nanoen.2023.108662.

[70] O. Younas, P. Li, Y. Wen, Self-powered piezoelectric energy harvesting with ultra-low power consumption for low-amplitude ambient vibrations, J. Power Electron. 24 (6) (2024) 853–861, https://doi.org/10.1007/s43236-024-00766-9.

[71] L. Wang, C. Duan, C. Li, Q. Wang, H. Huang, D. Ju, H. Liu, X. Han, L. Zhao, Z. Jiang, R. Maeda, Multi-frequency piezoelectric vibration energy harvesters powered sensing in power grid transformer, PREPRINT (Version 1) available at Research Square, https://doi.org/10.21203/rs.3.rs-3736998/v1, 2024.

[72] S.N. Shevtsov, A.N. Soloviev, I.A. Parinov, A.V. Cherpakov, V.A. Chebanenko, Piezoelectric Actuators and Generators for Energy Harvesting: Research and Development, SpringerLink Bücher, Springer, Cham, 2018.

[73] R. Fromm, L. Schott, F. Derbel, An efficient low-power wake-up receiver architecture for power saving for transmitter and receiver communications, in: International Conference on Sensor Networks, 2021, pp. 61–68.

[74] M.K. Baazaoui, I. Ketata, A. Fakhfakh, F. Derbel, Modeling of packet error rate distribution based on received signal strength indications in omnet++ for wake-up receivers, Sensors 23 (5) (2023) 2394, https://doi.org/10.3390/s23052394.

[75] M. Weber, G. Fersi, F. Derbel, Wake-up receiver based routing protocol for indoor wireless sensor networks, in: M. Charalambides (Ed.), Proceedings of the 18th International Conference on Network and Service Management, ACM Digital Library, International Federation for Information Processing, Laxenburg, Austria, 2022, pp. 289–295.

[76] L. Schott, R. Fromm, G. Bouattour, O. Kanoun, F. Derbel, Analytical and experimental performance analysis of enhanced wake-up receivers based on low-power base-band amplifiers, Sensors 22 (6) (2022), https://doi.org/10.3390/s22062169.

[77] R. Thiel, F. Strakosch, Zur vorbeugenden instandhaltung von planetengetrieben mit beschleunigungssensoren in den planetenrädern, in: N. Günther, B. Prell, R. van de Sand, J. Reiff-Stephan (Eds.), Industrie 5.0 Lernumgebung Am Beispiel der Wildauer Smart Production, Hochschule Für Technik Wirtschaft und Kultur, Leipzig, Leipzig, 2024, pp. 11–20.

[78] F. Strakosch, H. Nikoleizig, F. Derbel, Analysis and evaluation of vibration sensors for predictive maintenance of large gears with an appropriate test bench, in: To Measure Is to Know, IEEE, Piscataway, NJ, USA, 2021, pp. 1–6.

[79] K. Uchino, 1 - the development of piezoelectric materials and the new perspective, in: K. Uchino (Ed.), Advanced Piezoelectric Materials: Science and Technology, Woodhead Publishing Series in Electronic and Optical Materials, Woodhead Publishing, 2010, pp. 1–85.

[80] S.G. Kelly, S.G. Kelly, Schaum's Outline of Theory and Problems of Mechanical Vibrations, Schaum's Electronic Tutor, McGraw-Hill, New York, 1996.

[81] A.H. Meitzler, Ieee standard on piezoelectricity, ANSI/IEEE Std 176-1987, 1987.

[82] C. Covaci, A. Gontean, Piezoelectric energy harvesting solutions: a review, Sensors 20 (12) (2020) 3512, https://doi.org/10.3390/s20123512.

[83] H. Liu, C.J. Tay, C. Quan, T. Kobayashi, C. Lee, Piezoelectric mems energy harvester for low-frequency vibrations with wideband operation range and steadily increased output power, J. Microelectromech. Syst. 20 (5) (2011) 1131–1142, https://doi.org/10.1109/JMEMS.2011.2162488.

[84] T.M. Kamel, R. Elfrink, M. Renaud, D. Hohlfeld, M. Goedbloed, C. de Nooijer, M. Jambunathan, R. van Schaijk, Modeling and characterization of mems-based piezoelectric harvesting devices, J. Micromech. Microeng. 20 (10) (2010) 105023, https://doi.org/10.1088/0960-1317/20/10/105023.

[85] M. Zhu, E. Worthington, J. Njuguna, Analyses of power output of piezoelectric energy-harvesting devices directly connected to a load resistor using a coupled piezoelectric-circuit finite element method, IEEE Trans. Ultrason. Ferroelectr. Freq. Control 56 (7) (2009) 1309–1318, https://doi.org/10.1109/TUFFC.2009.1187.

[86] R.W. Martin, R.A. Sigelmann, Force and electrical thevenin equivalent circuits and simulations for thickness mode piezoelectric transducers, J. Acoust. Soc. Am. 58 (2) (1975) 475–489, https://doi.org/10.1121/1.380693.

[87] Y. Li, X. Hou, W. Qi, Q. Wang, X. Zhang, Modeling and analysis of multiple attached masses tuning a piezoelectric cantilever beam resonant frequency, Shock Vib. 2020 (2020) 1–12, https://doi.org/10.1155/2020/6971983.

[88] C. Săvescu (Borzea), C.D. Comeaga, Adjusting the resonant frequency of a cantilever piezoelectric harvester, Sci. J. TURBO V (2) (2018), https://doi.org/10.1088/0964-1726/23/8/085002.

[89] Y. Jia, A.A. Seshia, Power optimization by mass tuning for mems piezoelectric cantilever vibration energy harvesting, J. Microelectromech. Syst. 25 (1) (2016) 108–117, https://doi.org/10.1109/JMEMS.2015.2496346.